Bridging Microscopic Dynamics and Hydraulic Permeability in Mechanically-Deformed Nanoporous Materials

Alexander Schlaich, Matthieu Vandamme, Marie Plazanet, Benoit Coasne

Bridging Microscopic Dynamics and Hydraulic Permeability in Mechanically-Deformed Nanoporous Materials

Alexander Schlaich,[*,†,‡,¶] Matthieu Vandamme,[§] Marie Plazanet,[¶] and Benoit Coasne[*,¶,‖]

† *Stuttgart Center for Simulation Science (SC SimTech), University of Stuttgart, 70569 Stuttgart, Germany*

‡ *Institute for Computational Physics, University of Stuttgart, 70569 Stuttgart, Germany*

¶ *Univ. Grenoble Alpes, CNRS, LIPhy, 38000 Grenoble, France*

§ *Navier, Ecole des Ponts, Univ. Gustave Eiffel, CNRS, Marne-la-Vallée, France*

‖ *Institut Laue Langevin, F-38042 Grenoble, France*

E-mail: alexander.schlaich@simtech.uni-stuttgart.de; benoit.coasne@univ-grenoble-alpes.fr

Abstract

In the field of nanoconfined fluids, there are striking examples of deformation/transport coupling in which mechanical solicitation of the confining host and dynamics of the confined fluid impact each other. While this intriguing behavior can be potentially used for practical applications (e.g. energy storage, phase separation, catalysis), the underlying mechanisms remain to be understood as they challenge existing frameworks. Here, using molecular simulations analyzed through concepts inherent to interfacial fluids, we investigate fluid flow in compliant nanoporous materials subjected to external mechanical stresses. We show that the pore mechanical properties significantly affect fluid

flow as they lead to significant pore deformations and different density layering at the interface accounted for by invoking interfacial viscous effects. Despite such poromechanical effects, we show that the thermodynamic properties (i.e. adsorption) can be linked consistently to Darcy's law for the permeability by invoking a pore size definition based on the concept of Gibbs' dividing surface. In particular, regardless of the pore stiffness and applied external stress, all data can be rationalized by accounting for the fluid viscosity and slippage at the interface independent of a specific pore size definition. Using such a formalism, we establish that the intimate relation — derived using the linear response theory — between collective diffusivity and hydraulic permeability remains valid. This allows for linking consistently microscopic dynamics experiments and permeability experiments on fluid flow in compliant nanoporous materials.

Fluid/solid interfaces, which are inherent to vicinal and confined liquids as encountered in nanofluidic devices and nanoporous materials, are host to a wealth of molecular mechanisms such as adsorption and chemical reactions, but also to electrokinetic aspects (electrical double layer, crowding, etc.).[1–6] With the boost in nanosciences and nanotechnologies, these specific surface phenomena are already implemented in important applications such as energy storage, catalysis, lubrication or depollution.[7–11] Yet, despite significant progress in our understanding of surface forces and confinement effects on the thermodynamics and dynamics of fluids, the behavior of nanoconfined systems still challenges existing frameworks even when simple liquids are considered. Among important aspects that remain to be understood, there are now important experimental and numerical reports on the role of mechanical deformation on transport of gases and liquids in nanoconfined environments.[12–16] Formally, the coupling between mechanics of the confining host and dynamics of the confined fluid can manifest itself at various scales and in different fashions. Locally, i.e. at the fluid/solid interface, momentum transfer between phonons in the solid phase and molecules in the fluid phase are expected to give rise to complex surface thermodynamic and dynamical aspects.[13,15,16] At the pore scale and beyond, mechanical deformation of the pore network drastically impacts the fluid microscopic dynamics and, in turn, its macroscopic permeability.[17–21]

Originally, despite the complexity of biological channels and biological objects in general, biology is an important field in which fascinating mechano-transport mechanisms were identified. Detailed investigation on ionic channels and lipid membranes have unraveled complex phenomena such as the mechanotransduction response of ionic transfer upon mechanical or pressure solicitation.[22] First systematic efforts to stimulate such coupling employed man-made nanochannels (carbon nanotubes).[12] Recently, using single digit experiments on carbon nanotubes, Marcotte et al. were able to reproduce mechanically activated ionic transport.[15] Using 2D nanoporous membranes, Noh and Aluru used molecular dynamics simulations displaying a striking impact of membrane mechanics on water desalination.[16] Depending on the deformation amplitude and frequency, these authors observed a drastic effect on water permeability accompanied by a small decrease in salt rejection. By analyzing in detail the dynamics of the deformable membrane and vicinal water, the vibrational matching between the membrane and water molecules was found to be the key factor governing the resulting flow. Despite the important works cited above, several key questions remain left unanswered. In particular, while available data point to the phonon–fluid coupling as the origin of flow modifications, the exact role of mechanical deformation — including its quantitative impact — remains to be assessed. In particular, the validity of the intricate connection between permeability — as defined in macroscopic experiments such as in Darcy's law — and the collective microscopic diffusivity remains to be established when mechanical solicitation is applied. Extending such formalism to porous materials and, in particular, to nanoporous solids is an important step to design mechanical control and stimulation of fluid adsorption and flow in confined geometries.

Darcy's law for fluid flow through a porous medium has originally been proposed for macroscopic permeability measurements.[23] Yet, it can be rigorously derived from fundamental conservation laws, i.e. the Navier–Stokes equations.[24,25] In detail, in the case of a single-phase fluid considered here (assumed to be confined in the z-direction), one considers

the molecular flux

$$J = \int_{-L_z/2}^{L_z/2} \rho(z) v(z) \, \mathrm{d}z \tag{1}$$

induced by a pressure gradient ∇P, where $\rho(z)$ is the local fluid molecular density and $v(z)$ its corresponding velocity. The integration boundaries denote a length-scale L_z, which corresponds to the domain size. If the density is taken to be homogeneous, this molecular flux $J = \rho\bar{v}$ corresponds to a flow rate (mean velocity) $\bar{v} = -k/\eta \nabla P = -K\nabla P$, where η is the fluid viscosity, k the permeability and $K = k/\eta$ the (hydraulic) permeance.[25,26] Direct assessment of K is difficult in general in molecular simulations since a constant pressure gradient simulation needs to be set-up,[27–29] requiring for explicit treatment of reservoirs and therefore also introducing surface effects.[30] On the other hand, Onsager's relation $J = -D_0/\left(k_\mathrm{B}T\right) \times \nabla\mu$ relates the flux to the chemical potential gradient $\nabla\mu = -f_x$ in the direction x of the flow (k_B and T are the Boltzmann constant and temperature, respectively). The latter situation can be directly considered in molecular simulations through the measurement of the collective diffusivity D_0 as a response to a constant force f_x. A general approach to relate the transport coefficients due to different driving forces was developed by Onsager.[31] To relate the above Darcy and Onsager laws, an incompressible liquid is usually assumed for which we can use straightforwardly the Gibbs–Duhem equation: $\rho \, \mathrm{d}\mu = \mathrm{d}P$ (which therefore relates the pressure and chemical potential gradients as driving forces). In so doing, one obtains the following classical result for an incompressible fluid:[32]

$$K = D_0/\left(\rho k_\mathrm{B} T\right). \tag{2}$$

Previous studies have considered density-dependence of diffusion,[33–36] spatial density and viscosity heterogeneity,[29,37] and the the influence of pore size[38,39] or flexibility on transport.[14,16] Here, we report on a molecular simulation and theoretical approach to investigate the coupling between mechanical load and flow permeability. Using a simple yet representative model of nanoporous materials, we design a set-up in which the flow of water induced

by a driving force (pressure gradient) is monitored as a function of the mechanical stress applied in a direction perpendicular to the pore surface. To assess the validity of our results, both equilibrium and non-equilibrium molecular dynamics are employed; using a fluctuation-dissipation approach based on the Green–Kubo formalism allows verifying that the data and analysis are not biased due to unphysical coupling between the flow and deformation when driving forces are applied in non-equilibrium molecular dynamics. For different pore sizes and mechanical loadings, we analyze the role of the external mechanical stimulus (stress) and pore mechanical property (stiffness) on the system's response — both the resulting flow and mechanical deformation are analyzed simultaneously to unravel their interplay. The advective transport of confined water under mechanical solicitation is then analyzed through the prism of the fundamentals of interfacial fluids as developed in the field of nanofluidics and fluids confined in nanoporous materials. This allows us to probe the origin of the impact of mechanical deformation on flow through its effect on the interfacial viscous layer. Using the linear response theory and the underlying fluctuation-dissipation theorem, we show that — akin to non-compliant porous materials — the macroscopic permeability can be linked to the microscopic collective diffusivity as probed using simple molecular simulation. Beyond verifying its validity for compliant systems, this fundamental relation provides a means to define the pore size that consistently describes both the thermodynamics and dynamics of the confined fluid. In particular, using excess quantities as defined in the Gibbs dividing surface formalism, our data for the collective diffusivity and permeability are found to quantitatively match.

Our setup consists of a compliant slit pore composed out of a realistic dense and hydrophobic carbon material.[40] The two pore walls separated by a distance H between the outermost carbon atoms are treated as a rigid body and connected by a Hookean spring of stiffness κ_{zz} acting between the center of mass (COM) of the pore walls, see Fig. 1(a) and Section II of the Supplementary Information. While the left wall in Fig. 1(a) is fixed in space, the right wall is allowed to fluctuate freely and to respond to an external stress in

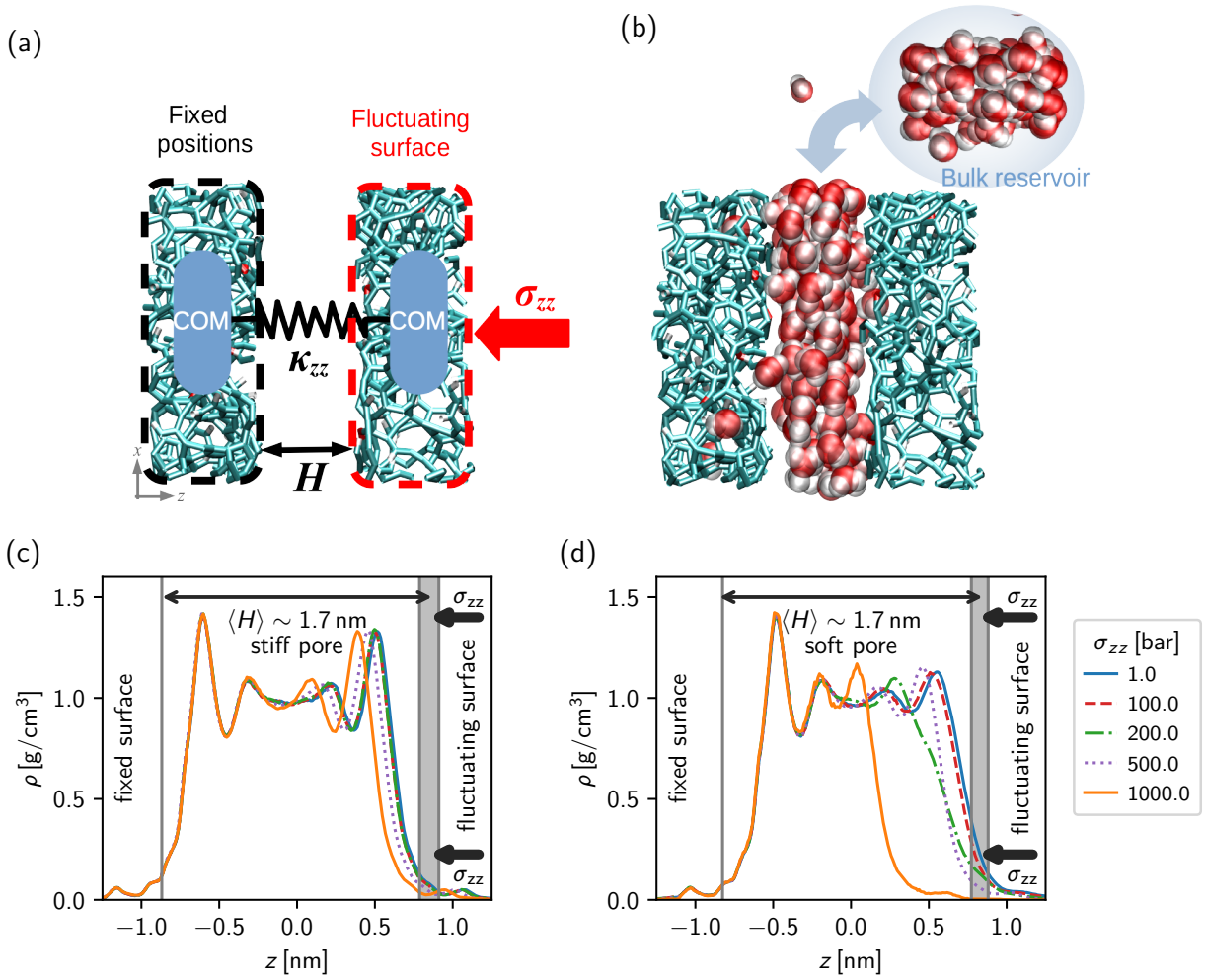

FIG. 1: **Adsorption in compliant nanoporous materials.** (a) Set-up of the compliant slit-pore considered in this study. The positions of the left pore wall atoms are kept fixed whereas the right pore wall is allowed to move as a rigid body. The two pores are connected via a Hookean spring of stiffness κ_{zz} acting between their respective centers of mass (COM) and several κ_{zz} are considered to tune the mechanical pore properties. An external stress σ_{zz} is applied as a body force acting on the fluctuating surface. For a given spring constant k, depending on the chemical potential of the external reservoir, the pore gets filled as indicated in (b). The resulting surface-to-surface separation fluctuates with an average position $\langle H \rangle$ defined as the distance from the planes passing through the atom centers at the wall external layer as indicated in (a). (c) and (d) show water density profiles for a slit pore with $\langle H \rangle \sim 1.7\,\text{nm}$ for a stiff (c) and soft (d) compliant material for different applied external stresses σ_{zz}. The chemical potential μ is fixed to a value corresponding to a pressure of about 215 bar to ensure all pores are filled. The vertical solid bars, which indicate the positions of the lower and upper walls, define the pore spacing H (the left wall is fixed so that its position does not fluctuate). For $\sigma_{zz} = 1000\,\text{bar}$ in (d) one water layer gets expelled, leading to a reduction of the pore size from 1.6 nm ($\sigma_{zz} = 500\,\text{bar}$) to 1.25 nm.

$\sigma_{zz} = f_z N_s/(L_x L_y)$ in the z-direction normal to the surface (such an external constraint is applied via a force f_z that acts on all N_s surface atoms with $L_x = L_y = 2.5\,\mathrm{nm}$ the lateral dimensions of the periodic simulation box). The harmonic potential $V(l) = \kappa_{zz}(l - l_0)^2$, which depends on the spring extension l, can be related to the slit pore's young modulus, $E_{zz} = \kappa_{zz} l_0/(L_x L_y)$, where l_0 is the equilibrium length between the wall's COM resulting in the pore width H, see Figure S1 in the Supporting Information. To mimic water exchange with the bulk external environment as indicated in Fig. 1(b), we perform Grand-Canonical Monte-Carlo (GCMC) and Molecular Dynamics (MD) simulations using the LAMMPS simulation package, all details are given in Methods. In line with intrusion experiments in such hydrophobic materials, the water chemical potential is chosen such that its bulk pressure corresponds to $P_0 = 215\,\mathrm{bar}$, see Section III of the Supplementary Information.

We study two systems: (i) a non-compliant pore ($E_{zz} = \infty$) and (ii) a compliant system, which can swell upon water adsorption. For the compliant case, we consider two values for the pore modulus, $E_{zz} = 0.2$ and 2 GPa. Then, in a second step, for the compliant systems we explicitly address the impact of pore size fluctuations on water transport through these pores. In detail, we let the pore relax to its equilibrium size in the presence of water, but then fix it to its average value $\langle H \rangle$. In so doing, we keep the thermodynamic state of the confined water and can study the influence of fluctuating and non-fluctuating pore walls (by fixing the pore size H to $\langle H \rangle$ or by letting H fluctuate around $\langle H \rangle$).

Adsorption and swelling in compliant nanoporous materials

The density profiles shown in Fig. 1(c) and (d) reveal significant layering at the surface fixed in space (left walls).[41–43] Similarly, layering is also observed — albeit less pronounced — for the stiff pore ($E_{zz} = 2\,\mathrm{GPa}$) shown on the right side of Fig. 1(c), where the data shows that the application of an external stress leads to expulsion of confined water and stronger layering effects. For the softer pore ($E_{zz} = 0.2\,\mathrm{GPa}$), the data shown on the right side of Fig. 1(d) show that surface fluctuations smear out the layering at the fluctuating

surface. Upon increasing the stress σ_{zz} in the range from 1 to 1000 bar, the water density profiles change significantly since the average pore separation is able to adjust to the water structure. At $\sigma_{zz} = 1000$ bar, in the case of the soft pore, we observe a transition in the profiles corresponding to the expulsion of one water layer, corresponding to a jump in pore size from about 1.6 nm at 500 bar to roughly 1.25 nm at 1000 bar. The data shown for that case correspond to an equilibrium length of the spring of $l_0 = 2.84$ nm, which is the largest value considered in this work.

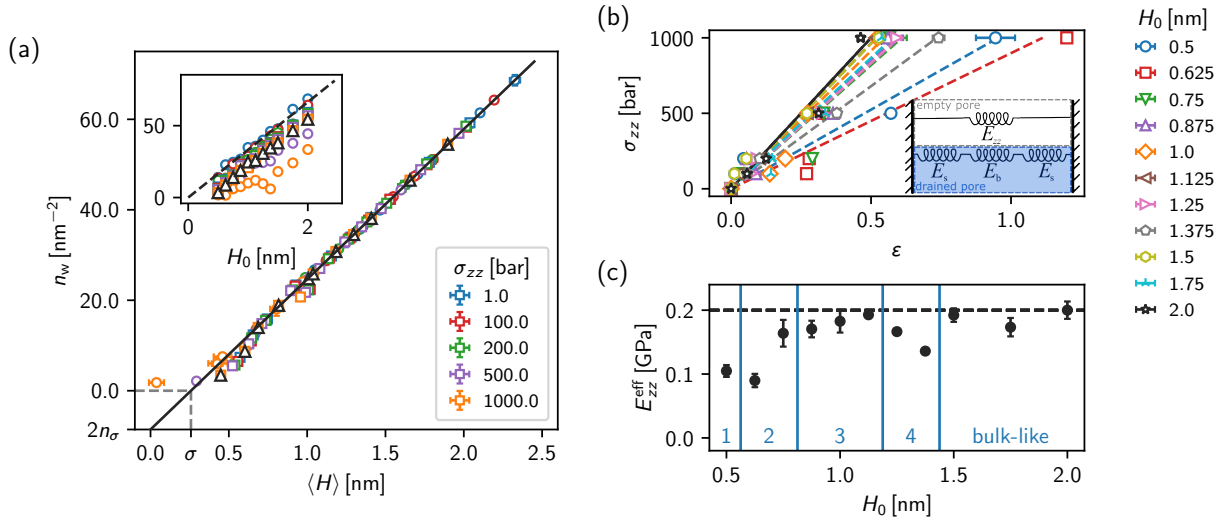

FIG. 2: **Water confinement and pore swelling in compliant nanoporous materials.** (a) Water surface density in molecules/nm^2 as obtained using GCMC simulations for the soft ($E_{zz} = 0.2$ GPa, circles) and stiff ($E_{zz} = 2$ GPa, squares) compliant nanoporous material at different external stresses σ_{zz}. Black triangles denote the simulation data for a non-compliant, i.e. infinitely stiff, nanopore. The black line corresponds to the expected variation based on the bulk water density taking into account excess surface density n_σ. The inset shows the same data versus the equilibrium pore size H_0 as obtained in the absence of any fluid. The dashed line shows the slope expected from the bulk water density. (b) Stress-strain relation for soft pores, $E_{zz} = 0.2$ GPa, with different nominal pore size H_0 as indicated by the legend on the right. Dashed lines denote fits of the effective modulus according to $\sigma_{zz} = \varepsilon E_{zz}^{\text{eff}}$. The solid line denotes the empty pore mechanical response without any effect due to adsorbed water, $\sigma_{zz} = \varepsilon E_{zz}$. The inset shows the equivalent circuit model as discussed in the text. (c) Effective modulus of the soft system for different equilibrium pore sizes obtained from the fits in (b). The vertical lines denote the different regimes, where in the density profiles 1-4 water layers can be observed. Above ~ 1.4 nm the water in the center of the slab is bulk-like, *cf.* Supplementary Figures 3 and 4.

To further quantify water adsorption in the compliant material, we show in Fig. 2(a) the

mean number of water molecules in the slit nanopore normalized to the lateral area of the pore, $n_\mathrm{w} = N_\mathrm{w}/\left(L_x L_y\right)$. The dashed line corresponds to the bulk water molecular volume, $n_\mathrm{w}/\langle H\rangle = 33.2\,\mathrm{nm}^{-3}$.[37] The inset of Fig. 2(a) shows the areal water number as a function of the equilibrium pore size in the absence of any fluid, which follows from the initial choice of the length of the harmonic spring, $H_0 = l_0 - 0.84\,\mathrm{nm}$ that connects the walls' COM. For a non-compliant, i.e. frozen, pore (black triangles), the slope corresponding to the bulk density is well reproduced, but with a shift z_G in the surface position corresponding to the Gibbs Dividing Surface.[44] In detail, the latter is defined for a single interface via the water surface excess with respect to its bulk phase,

$$z_\mathrm{G} = z_a + \int_{z_a}^{z_b} \frac{\rho(z_b) - \rho(z)}{\rho(z_b) - \rho(z_a)}\,\mathrm{d}z, \tag{3}$$

where $\rho(z_a) \sim 0$ and $\rho(z_b) = \rho_\mathrm{b}$ are the corresponding fluid densities far from both sides of the interface, i.e. no water inside the solid and water bulk density in the fluid phase. For the compliant pores (squares and circles), either swelling or compression is observed depending on the mechanical load applied, cf. inset of Fig. 2(a). All simulation data collapse to a master curve in Fig. 2(a) when the average effective pore separation $\langle H\rangle$ — defined as the distance between the outermost surface atoms — is employed. The excellent agreement in the slope observed for different surfaces stresses when large separations are considered reveals that nanoconfined water is nearly incompressible with a density that sufficiently away from the interface corresponds to the bulk density. According to Gibbs adsorption theory, we determine the surface excess defined for a single interface as

$$n_\sigma = \int_{-\infty}^{z_\mathrm{G}} \left[\rho(z) - \rho(z_a)\right]\,\mathrm{d}z + \int_{z_\mathrm{G}}^{\infty} \left[\rho(z) - \rho(z_b)\right]\,\mathrm{d}z. \tag{4}$$

This can be conveniently done for confined system by fitting fitting the offset of the line corresponding to bulkd density to all simulation data for which $\langle H\rangle > 1\,\mathrm{nm}$ in Fig. 2(a) and yields $2n_\sigma = -8.6\,\mathrm{nm}^{-2}$. Such a negative value indicates that water is depleted from

the hydrophobic surface. This result was expected for the hydrophobic surface chemistry studied here which leads to non-favorable fluid/solid interactions. The associated surface separations $\langle H \rangle < \sigma$ at which the slit pore accommodates no water molecules, $\sigma = 2.65\,\text{Å}$, perfectly coincides with the water kinetic diameter (which is related to the mean free path of molecules in a fluid phase).[45]

The change of pore size upon external mechanical stimulation can be further analyzed by determining the stress-strain relation in Fig. 2(b) For all systems considered, we find the strain $\varepsilon = (H_0 - \langle H \rangle)/H_0$ to be roughly related linearly to the normal stress σ_{zz}, where here, per convention, a shrinkage corresponds to a positive strain. This is not necessarily the expected behavior since the interfacial structure and compressibility of water are non-negligible for the small pores considered. However, the strain-stress linearity allows us to extract the apparent (effective) modulus of the slit pore under drained conditions, $E_{zz}^{\text{eff}} = \sigma_{zz}/\varepsilon$, in analogy to the apparent tangent drained bulk modulus derived from a generalized poromechanics framework.[46] The corresponding equivalent circuit depicted in the inset of Fig. 2(b) consists of the mechanical properties of the empty pore, characterized through the modulus E_{zz} acting in parallel with the water mechanical response under drained conditions. In fact, the latter can be further dissected into the water bulk and surface contributions, E_{b} and E_{s}, respectively, acting in series (as the total strain upon application of a normal stress σ_{zz} must be equal to the sum of the strains of the individual springs). The corresponding effective modulus follows as

$$E_{zz}^{\text{eff}} = E_{zz} + \frac{1}{E_{\text{b}}^{-1} + 2E_{\text{s}}^{-1}}. \tag{5}$$

If we assume a linear relation to hold, linear fits to the simulation data in Fig. 2(b) allow for the determination of the effective Young modulus in presence of water, $E_{zz}^{\text{eff}} = \sigma_{zz}/\varepsilon$.[47,48] Such data are shown in Fig. 2(c) for the soft compliant pore with $E_{zz} = 0.2\,\text{GPa}$. For sufficiently large separations $H_0 \gtrsim 1.5\,\text{nm}$, interfacial effects (at sufficiently large strain, see Fig. 2(b)) become negligible if the water is allowed to exchange with the reservoir. In that case, $E_{zz}^{\text{eff}} \sim E_{zz}$ is recovered, i.e. the response to an applied stress of the filled pore sys-

tem corresponds to that of the confining material. Since the water bulk modulus is about 25 kbar,[49] this implies that the term $2E_{\mathrm{s}}^{-1}$ dominates the denominator in Eq. (5), i.e. the surface layer modulus must be small such that the total fraction vanishes. Further analysis of the data shown in Fig. 2(c) for the soft pore and in Figure S2 in the Supplementary Information for the stiff pore reveals that $E_{zz}^{\mathrm{eff}} \lesssim E_{zz}$. Since E_{b} is positive and independent of the pore width, this indicates that E_{s} depends on H_0 and E_{zz}, and is negative. Although this is a counterintuitive result at first (since it indicates a negative apparent surface compressibility), it is in line with generalized poromechanics stating that the apparent tangent bulk modulus can be smaller than its counterpart in bulk depending on the adsorption properties.[46] Physically, it corresponds to the concept of a disjoining pressure,[50] which depending on the wetting properties either is attractive or repulsive.[51] Note, that the typical signature of hydration forces — the oscillatory stress vs. pore size curve — is encapsulated in the effective modulus since the pore can mechanically adapt to the molecular water structure.

Interestingly, deviations for the smaller pores with $E_{zz}^{\mathrm{eff}} \neq E_{zz}$ can be correlated with the density layering shown in Fig. 1 (Figures S3 and S4 in the Supplementary Information show the same data for all systems). The vertical blue lines in Fig. 2(c) indicate the corresponding number of water layers. For $H_0 \gtrsim 1.5\,\mathrm{nm}$, the water density profile in the slit pore center becomes homogeneous and equal to its bulk value (so that density heterogeneities correspond to two distinct layers at the solid/fluid interface). Depending on the pore separation H, in the case of the smaller pores, water organizes into one, two, three or four layers. Moreover, significant deviations from the prescribed modulus can be observed. The exact influence of the interfacial contribution depends sensitively on the equilibrium surface separation $\langle H \rangle$ of the system in contact with the reservoir. It also depends on the applied mechanical stress σ_{zz} which strongly affects the thermodynamic state of nanoconfined water. Indeed, even if confined water in each system is at the same chemical potential μ and temperature T, its thermodynamic state also depends on the prescribed mechanical condition σ_{zz}.

Transport in compliant nanoporous materials

Collective diffusivity. Having assessed the thermodynamic and adsorption behavior of water in compliant slit nanopores, we now turn to transport in the presence of a fluctuating interface. We first focus on Onsager flow, where the universal thermodynamic driving force is a gradient in the chemical potential, $\nabla\mu$. Solving Eq. (1) for the mean velocity $\bar{v}$ while taking into account the heterogeneous density distribution $\rho(z)$ yields

$$\bar{v} = \frac{\int \rho(z) v(z)\,\mathrm{d}z'}{\int \rho(z)\,\mathrm{d}z'} = -\frac{D_0}{k_\mathrm{B}T}\nabla\mu \tag{6}$$

where Onsager's relation defined in Eq. (2) was used. Eq. (6) rigorously defines D_0 from the velocity $v(z)$ and density $\rho(z)$ profiles without any need of defining a pore size H or homogeneous density ρ. This is a significant advantage in the definition of D_0, which can be probed experimentally — e.g. using quasi-elastic coherent neutron scattering. In contrast, the permeance K defined in Darcy's equation relies on the ambiguous definition of a pore size as discussed below.

In the following, we unravel the effect of pore elasticity by limiting the discussion to the specific case where the external stress is set to $\sigma_{zz} = 1\,\mathrm{bar}$. Equation (6) provides a means to directly determine D_0 from non-equilibrium simulations, where a chemical potential gradient in the x-direction parallel to the pore is applied via a homogeneous force field acting on each water molecule, $\nabla\mu = -f_x$, see Methods for details. Figure 3 shows the resulting mean velocity which can be obtained directly from the density and velocity profiles according to Eq. (6). In the case of point particles, the flow rate can be further simplified to $\bar{v} = 1/\tau \int_0^\tau \mathrm{d}t\, 1/N_\mathrm{w} \sum_{i=0}^{N_\mathrm{w}} v_i(t)$, where $v_i(t)$ denotes the instantaneous velocity of a water molecule's center of mass in the direction of the flow at time t and the integral averages over the simulation time τ.

Figure 3(a) shows $\bar{v}$ as a function of the driving force $f_x = -\nabla\mu$ for different pore widths $\langle H \rangle$ and stiffnesses E_{zz}. Whereas Eq. (6) is intrinsically a linear relation, the linear response

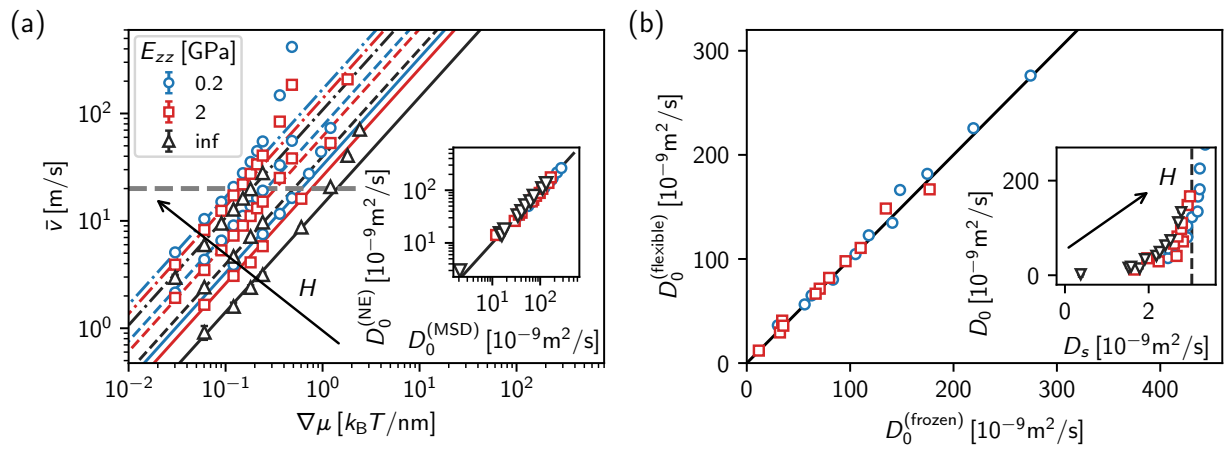

FIG. 3: **Probing dynamics in equilibrium and non-equilibrium conditions.** (a) Typical fits for the mean water velocity $\langle v \rangle$ vs. driving force $\nabla\mu$. Color code corresponds to the stiffness as shown in legend. Data are shown for three characteristic pore sizes $H \approx 0.75\,\mathrm{nm}$ (solid lines), 1.25 nm (dashed lines) and 1.75 nm (dashed-dotted lines). The inset shows the collective diffusion coefficient determined from the linear response regime of the mean water velocity (non-equilibrium molecular dynamics) vs. the collective diffusion coefficient determined from the mean-squared displacement (equilibrium molecular dynamics). All values for the flexible pores are shown for $\sigma_{zz} = 1\,\mathrm{bar}$. (b) Diffusion coefficient in flexible pores vs. frozen pores (same mean pore size and water number but non-fluctuating walls). The black line indicates the bisector for clarity. The inset shows the collective diffusion constant D_0 vs. the self-diffusion coefficient D_s to display the role of collective contributions (cross-terms) in diffusion. The vertical dashed line corresponds to the bulk value $D_\mathrm{s}^{(\mathrm{b})} = 3.03\,\mathrm{m}^2/\mathrm{s}$ determined from independent simulations with finite size scaling, see Section IV of the Supplementary Information for details.

regime is not achieved in the molecular simulations (as well as in experiments) when too large driving forces are used. However, we find that for sufficiently small driving forces the linear response limit can be probed [lines in Fig. 3(a)]. In particular, the interfacial friction between water and the surface governs the onset of nonlinear effects. As a result, the critical driving force at the crossover between the linear and nonlinear regimes sensitively depends on the surface separation as well as the pore flexibility.[37] The frictional stress at the interface increases with $\bar{v}^3$ within the classical Darcy-Weisbach theory. This explains the emergence of a critical value $\bar{v}_\mathrm{crit} = 20\,\mathrm{m/s}$ which is rather independent of the pore size and stiffness. Such a velocity cutoff for the linear response regime can be rationalized with an activated diffusion of water molecules over barriers at the interface.[52] Note that, however, the corresponding

driving forces are highly dependent on the pore size, which is in line with the expectation from classical Hagen-Poiseuille theory.

In practice, we fit $D_0^{(\mathrm{NE})}$ in Eq. (6) to the non-equilibrium simulation data in Fig. 3(a) for velocities $\bar{v} < \bar{v}^{\mathrm{crit}}$. The fits are indicated as black and color lines, whereas the horizontal dashed gray line in Fig. 3(a) denotes the employed value $\bar{v}^{\mathrm{crit}} = 20\,\mathrm{m/s}$. As shown in the inset of Fig. 3(a), the obtained values are in perfect agreement with the equilibrium molecular dynamics results relying on the mean-squared displacement and the fluctuation-dissipation theorem, see Methods and Figures S7 and S8 in the Supplementary Supplementary Information. As can be observed from the data in Fig. 3(a), the collective diffusion D_0 increases with pore size in line with a Poiseuille flow, but also with pore flexibility (black via red to blue data). To shed further light on the dependence $D_0(E_{zz})$, we performed an additional set of simulations at constant (non-fluctuating) pore size with a value fixed at $H = \langle H \rangle$, where the brackets denote the time-average of the fluctuating pore size for the specific stiffness E_{zz}. The resulting diffusion coefficients in Fig. 3(b) perfectly agree between the fluctuating and non-fluctuating pores with the same fixed water number N_{w}. This result points to the fact that D_0 depends on adsorption/layering rather than on pore size fluctuations. However, we note that the rather large pore size employed here together with the incompressibility of water and the employment of a stiff surface can explain the negligible impact of pore size fluctuations. In other words, for smaller pores (or, equivalently, larger surface to volume ratios), pore size fluctuations and, in general, mechanical deformations are expected to affect liquid flow in nanoconfinement. This point will be addressed further below.

The collective diffusivity as defined in Onsager's law, i.e. Eqs. (1) and (6), differs strongly from the self-diffusion coefficient D_{s} that follows from tracking a tagged molecule.[53] The collective correlations in a fluid are usually positive and thus strongly enhance D_0 compared to D_{s} (and in the dilute limit $D_0 \to D_{\mathrm{s}}$). The inset of Fig. 3(b) shows the corresponding relation D_0 vs. D_{s} for a confined system, for details on the calculation see Methods. Interestingly, due to interfacial depletion/adsorption effects, D_{s} in a confined system can also

become larger/smaller than its counterpart in bulk at the same chemical potential/pressure, $D_{\mathrm{s}}^{(0)} = 3.03\,\mathrm{m}^2/\mathrm{s}$, which we determined in independent simulations for our water model, see Section IV of the Supplementary Information. A detailed discussion of such effects is out of scope of this work and well represented in text books.[54]

Velocity profiles. Further insight can be obtained from analyzing the velocity and density profiles. To this end, we perform a coordinate transformation from the lab frame [Fig. 1(a)] into the pore frame, i.e. $z \to z - z_{\mathrm{COM}}(t)$, where $z_{\mathrm{COM}} = \sum_i [z_i(t) m_i] / \sum_i m_i$ is the fluctuating center of mass of the pore and the sum runs over all i pore wall atoms. The resulting density profiles, which are illustrated for the stiffer system and an average pore size $\langle H \rangle = 1.4\,\mathrm{nm}$ in Fig. 4(a), reveal that in this frame the density profiles are symmetric as expected. Furthermore, as already noted above, the first peak of the density profile is strongly depleted from the position of the interface (defined by the outermost position of the wall atoms). The velocity profile [purple data in Fig. 4(a)] is parabolic in the slab center and decays nearly linearly to zero at the pore wall, $z = H/2$. Importantly, the velocity profiles are perfectly in line with the solution of the Stokes flow in the presence of an interfacial fluid film of thickness w. The modified Poiseuille profile accounting for continuity of the velocity and stress at the interface between the two zones is given by

$$\begin{aligned} v_x(z) &= \frac{\nabla P}{2}\left[\frac{1}{\eta_{\mathrm{b}}}\left(a^2 - z^2\right) + \frac{1}{\eta_{\mathrm{s}}}\left(\frac{H^2}{4} - a^2\right)\right] && \text{for} \quad 0 \le |z| \le \frac{a}{2} \\ v_x(z) &= \frac{\nabla P}{2\eta_{\mathrm{s}}}\left[\frac{H^2}{4} - z^2\right] && \text{for} \quad \frac{a}{2} \le |z| \le H, \end{aligned} \tag{7}$$

where we introduced the width of the bulk-like region, $2a = H - 2w$ to simplify notation and η_{b} and η_{s} denote the bulk and surface layer effective viscosities, respectively. To apply Eq. (7) to our simulations involving a gradient in the chemical potential instead of the pressure, we make use of the Gibbs–Duhem relation for incompressible water ($\mathrm{d}P = \rho \mathrm{d}\mu$) to obtain $\nabla P = -f_x N_{\mathrm{w}} / (L_x L_y H)$.

Fits of Eq. (7) to the simulation data shown in Fig. 4 reveal excellent agreement with the

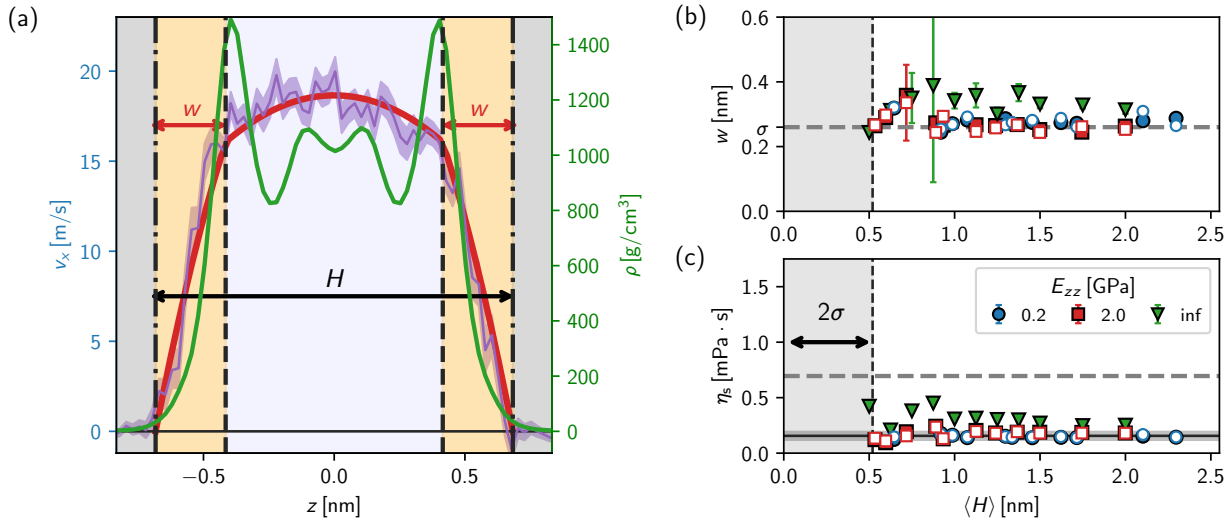

FIG. 4: **Velocity profiles and interfacial properties.** (a) Velocity (purple line) and density (green line) profiles in the pore-center coordinate frame (see text) obtained in the linear regime for the slit pore with $\langle H \rangle = 1.4\,\mathrm{nm}$ (indicated by the dash-dotted vertical black lines) and pore stiffness $E_{zz} = 2\,\mathrm{GPa}$. The red line denotes the fit against a two-zone Poiseuille flow accounting for an interfacial viscous layer, c.f. Eq. (7). The yellow shaded area denotes the fitted interfacial width w, the shaded area of the velocity profile the standard error of the mean. (b) Fitted values of the interfacial width and (c) viscosity for the different pore stiffnesses and sizes. The dashed horizontal line in (b) denotes the value $\sigma = 0.26\,\mathrm{nm}$ obtained via the surface excess in Fig. 2(a). The dashed horizontal line in (c) denotes the bulk value of the water model used in the simulations, $\eta_\mathrm{b} = 0.695\,\mathrm{mPa \cdot s}$, whereas the solid line and shaded area denote the averaged viscosity in the interfacial layer, $\eta_\mathrm{s} = 0.16 \pm 0.04\,\mathrm{mPa \cdot s}$. The filled symbols in (b) and (c) correspond to fluctuating pores whereas the empty symbols are obtained for frozen pores, which nearly perfectly overlap with the data for the fluctuating pores. For $\langle H \rangle \leq 2\sigma$, the viscous behavior is purely interfacial as indicated by the shaded areas in (b) and (c).

two-zone Poiseuille flow (see also Figures S3 and S4 in the Supplementary Information for all systems). These data show a rather universal value for the interfacial width $w \approx \sigma = 0.26\,\mathrm{nm}$, c.f. Fig. 4(b). To improve numerical stability during the fitting procedure, we fix $w = \sigma$ in the following discussion. This approach is justified since it leads to comparable root-mean-square error in the fits to the velocity profiles. The interfacial layer has a strictly reduced viscosity as shown in Fig. 4(c). As can be seen in Fig. 4(a), water is strongly depleted from the surface within the width w. This is believed to result in a reduced value of η_s that is quasi independent of pore stiffness and size for the compliant pores with a value $\bar{\eta}_\mathrm{s} = 0.16 \pm 0.04\,\mathrm{mPa\,s}$ [solid black line and corresponding shaded area in Fig. 4(c)]. Importantly, the results of the fitting procedure are independent of whether we consider fluctuating or non-fluctuating pores at the same pore size and water content [empty symbols in Fig. 4(b,c)]. Noteworthy, in the non-compliant nanopores, $E_{zz} = \infty$, i.e. when the pore cannot adapt to the water structure by any modification of the pore size, water layering is enhanced (Figure S3 in the Supplementary Information) and the interfacial viscosity converges only slowly for comparatively large pores $> 2\,\mathrm{nm}$ towards $\bar{\eta}_\mathrm{s}$.

As observed from Fig. 4(a), both the density and velocity profiles approach zero at the steric definition of the pore size H and the usual *no-slip* boundary conditions perfectly holds. In the pore center, at a distance larger than $\sigma = 0.26\,\mathrm{nm}$ from the surface, the velocity profile is parabolic by construction from Eq. (7). It is noteworthy that this parabolic region of width $H - 2\sigma$ is different from the thermodynamic pore size $H - \sigma$ as defined above from the Gibbs dividing plane. Since both the density and velocity decay quickly to zero at distances smaller than σ from the surface, this region barely contributes to the flux according to Eq. (1). Thus, it is tempting to introduce a coarse-grained model of a simple planar Poiseuille flow in the region $[-(H/2 - \sigma), (H/2 - \sigma)]$. Two questions naturally arise at this stage. First, what is the corresponding boundary condition at the pore surface, $v\,(\pm(H/2 - \sigma))$? Second, what is the contribution of the deviations from the parabolic profile in the vicinity of the surface to the overall flow? Since the fluid velocity does not vanish at the interface to the bulk-like

flow region, the *no-slip* boundary condition does not hold. In this case, a *slip* boundary condition is introduced instead with a characteristic slip length

$$b = \pm v_x(z_{\text{surf}}) / \left(\mathrm{d}v_x/\mathrm{d}z\right)_{z_{\text{surf}}} . \tag{8}$$

Defining b requires the knowledge of the position of the corresponding surface z_{surf}, where the hydrodynamic boundary condition is applied. There is no absolute natural choice for z_{surf} in the case of an atomistically resolved surface.[55] This has led to different choices in the literature ranging from definitions based on the shear-stress correlation function,[56,57] the use of the Gibbs' dividing surface, the repulsive contribution of the surface interaction,[58] or simply based on the position of the surface atoms.[59] All these definitions sensitively influence the numerical value inferred for the slip length b.

Based on the excellent description obtained above with the two-zone Poiseuille flow accounting for interfacial viscosity for the simulated velocity profiles, we here propose the effective *hydrodynamic* diameter $H - 2\sigma$. In so doing, accounting for slippage and an effective viscosity reproduces the bulk-like region of the simulation results. Such a coarse-graining approach — despite the question about its validity to be addressed below — significantly simplifies the analytical treatment of the flow profiles. In detail, the Poiseuille flow with slip is given by

$$v_x(z) = \nabla P \frac{H^{\star 2}}{8\eta} \left[1 + \frac{4b}{H^\star} - \left(\frac{2z}{H^\star} \right)^2 \right] , \tag{9}$$

where the asterisk denotes the — generally unknown — effective pore size. We now identify $H^\star = H - 2\sigma$ and consider only the velocities in the region $[-(H/2-\sigma), (H/2-\sigma)]$ — where the profiles shown in Fig. 4 and for all systems in Figures S3 and S4 in the Supplementary Information are parabolic. Concerning the width w of the interfacial layer, Eqs. (8) and (9) define the slip length $b = \eta_{\text{b}} / \left(2\eta_{\text{i}}\right) \times \left(Hw - w^2\right) / \left(H/2 - w\right)$. With this definition, using the values $w = \sigma$ and $\bar{\eta}_{\text{s}}$ for large H results in $b = 1.2 \pm 0.3\,\text{nm}$, cf. Figure S5 in the Supplementary Information.

Importantly, to obtain the above expression for b, we have redefined the pore size as the effective hydrodynamic pore size according to $H^\star = H - 2\sigma$. It is worth mentioning, that if the pore size $H^\star = H$ would be employed and only the parabolic part of the velocity profile were considered, both the slip length and the apparent viscosity $\eta_{\mathrm{app}} = \eta_{\mathrm{b}} + 2w/H \times (\eta_{\mathrm{i}} - \eta_{\mathrm{b}})$ become dependent on H.[60] Depending on the interfacial properties, η_{app} can be orders of magnitude larger than the bulk viscosity,[37,43,61,62] or significantly decrease,[63,64] as observed also for the hydrophobic surfaces considered here. In summary, our observations from the density and velocity profiles reveal the two following points. (1) The thermodynamic pore size as defined from Gibbs's dividing surface differs from a steric definition H by a the characteristic size of a water molecule, $\sigma = 2.65\,\text{Å}$. (2) At the length of a molecular size, one observes interfacial viscous effects, i.e. the pore size where bulk hydrodynamic behavior is found is $H - 2\sigma$. Note that this is only partially equivalent to claiming that the hydrodynamic pore size is $H - 2\sigma$ because one needs to take into account slippage. In such a coarse-grained model — besides the fact that in general the pore size cannot be rigorously defined such that the apparent viscosity needs to be fitted — one misses a part in the flux due to neglecting the interface layer. This contribution to the total flux is in general rather small as will be discussed below.

Pore size fluctuations. To address the underlying effects of pore size fluctuations in a flexible nanopore, we assume in the following that the pore size of a pore with spring equilibrium length H_0 filled with water can be described using a Gaussian distribution around the mean spring extension e given by $f(e; E_{zz}) = 1/\left(\varsigma\sqrt{2\pi}\right) \exp\left[-1/2\left(\left(e - \bar{e}\right)/\varsigma\right)^2\right]$ (the extension e is due to swelling and the variance is ς). Note that we dropped the dependence on the external stress since in the following we limit our discussion to $\sigma_{zz} = 1\,\text{bar}$. For all systems, we find that the fluctuations are well described by this mathematical form for $f(e)$, cf. inset of Fig. 5(a). Dropping the dependence on the modulus, the average pore size follows as $\langle H \rangle = H_0 + \int_{-\infty}^{\infty} e f(e)\,\mathrm{d}e$.

To ensure a compact presentation of the following discussion, we here employ the coarse-

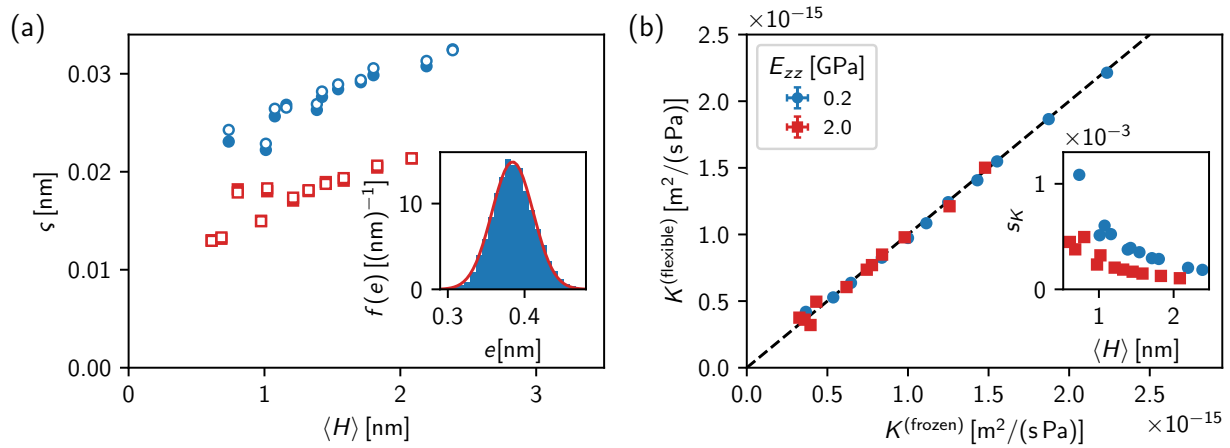

FIG. 5: **Influence of fluctuating vs. non-fluctuating pore surfaces.** (a) Variance of the pore size fluctuations in equilibrium (empty symbols) and non-equilibrium simulations (full symbols). The inset shows an example of the pore extension distribution function $f(e)$ for $E_{zz} = 0.2\,\mathrm{GPa}$ and $H_0 = 1\,\mathrm{nm}$, red line denotes a fit of a Gaussian to the data. (b) Permeance of the compliant, fluctuating pores vs. the respective value in a rigid pore at the same average pore size and particle number. The inset shows the expected relative permeability enhancement s_K due to pore size fluctuations (see text).

grained model presented above. In other words, the water velocity profiles in compliant pores can — neglecting interfacial effects — be modelled by a Hagen-Poiseuille law when accounting for slip and effective viscosity, see Eq. (9). An extension to the case where the interfacial viscous effects are treated explicitly is straightforward. A further simplification that is often made in the analysis of Darcy flows is to treat the water density $\rho = N_\mathrm{w}/V_\mathrm{w} = N_\mathrm{w}/(A\langle H\rangle)$ as homogeneous ($V_\mathrm{w} = A\langle H\rangle$ is the volume accessible to the water and $A = L_x L_y$ is the lateral area of the slit pore). Noting that the density profiles presented in Fig. 4 and for all systems in Figures S3 and S4 in the Supplementary Information are not homogeneous, we will discuss the limitations and impact of this simplification below. The permeance of a fluctuating nanopore with a Poiseuille velocity profile and slip follows from Eq. (9) as

$$K = \frac{\langle H^\star\rangle^2}{4\eta}\left(\frac{2b}{\langle H^\star\rangle} + \frac{1}{3}\right). \tag{10}$$

As discussed above, our NEMD simulations reveal that the slip length quickly approaches its asymptotic constant value $b = 1.2\,\mathrm{nm}$ for sufficiently large nanopores. Moreover, using

a consistent definition of the pore size, the viscosity $\eta = \eta_\mathrm{b}$ is found to be independent of $\langle H \rangle$ and pore fluctuations. Furthermore, employing $f(e)$ to express the mean pore size, we combine Eqs. (6) and (10) and perform the Gaussian integral, such that the collective diffusion coefficient can be expressed as

$$D_0 = k_\mathrm{B}T\langle \rho K \rangle = \frac{k_\mathrm{B}T}{6\eta} \frac{N_\mathrm{w}}{A\left(1 + \frac{2\sigma}{\langle H^\star \rangle}\right)} \langle H^\star \rangle \left(1 + \frac{3b}{\langle H^\star \rangle}\right), \tag{11}$$

which yields the important result of D_0 being independent of pore size fluctuations, in good agreement with the results presented in Fig. 3(b). Although being a first order approximation neglecting any fluid density heterogeneities or changes in the effective viscosity and slip, Eq. (11) captures remarkably well the qualitative behavior observed in the present work (see gray dashed line in Figure S6 in the Supplementary Information).

Plugging the pore size distribution using $f(e)$ into Eq. (1) allows us further to define the average flux according to $J = -\langle \rho v \rangle = -N_\mathrm{w}/\left(A\langle v/H \rangle\right)$. This directly yields the permeance for a fluctuating slit pore,

$$K = -\frac{A}{N\nabla\mu}\langle vH \rangle. \tag{12}$$

For a non-fluctuating pore $\langle vH \rangle = \langle v \rangle \langle H \rangle$ which yields the classical result $K^{(\mathrm{frozen})} = D_0/\left(k_\mathrm{B}T\right) \times A\langle H \rangle/N$. The latter expression relates the permeance and collective diffusion via the thermal energy and fluid density $\rho = N/\left(A\langle H \rangle\right)$. On the contrary, Eq. (12) reveals that a coupling between pore size fluctuations and the fluid velocity can impact transport in compliant pores (in contrast to the collective diffusivity which is expected to be independent of fluctuations as shown above). For the Poiseuille flow, the coupling can be made quantitative by calculating the second moment of the Gaussian integral appearing in Eq. (10), resulting to leading order in $K \sim H_0^2 + \int_{-\infty}^{\infty} e^2 f(e)\,\mathrm{d}e = \langle H \rangle^2 + \varsigma^2$, i.e. under these assumptions the fluctuations enhance transport in a fluctuating slit pore.

We show in Fig. 4(a) the variance ς of the pore size fluctuations determined both from equilibrium simulations, i.e. in the absence of flow, as well as from simulations with ap-

plied driving force $\nabla\mu$. Notably, EQMD and NEMD simulation results agree perfectly, revealing that flow does not affect the fluctuations in the linear response regime. Furthermore, fluctuations are in the range of about $(1-3)\times 10^{-2}\,\mathrm{nm}$ for the pore sizes $H \approx (0.5-2.5)\,\mathrm{nm}$ studied here, i.e. fluctuations are about two orders of magnitude smaller than the average pore size, which we attribute to the near-incompressibility of water under these thermodynamic and transport conditions. The resulting permeance $K^{(\mathrm{flexible})}$ obtained from NEMD simulations with fluctuating pores is plotted in Fig. 4(b) against the values $K^{(\mathrm{frozen})}$ obtained from simulations with the pore size fixed to the mean pore size $H = \langle H\rangle$ and same water number N_w (i.e. the positions of the surfaces were fixed). As expected from the small values of ς, the permeance K is quasi independent of the fluctuations. To quantify the expected flow enhancement due to pore fluctuations, we define the coefficient $s_K = \left(K^{(\mathrm{flexible})} - K^{(\mathrm{frozen})}\right)/K^{(\mathrm{frozen})} = \left(\langle H\rangle^2 + \varsigma^2\right)/\langle H\rangle^2$ shown in the inset of Fig. 5(b). We find values s_K as small as $10^{-3} - 10^{-4}$ for water in the studied slit pores, revealing that the impact of pore fluctuations on permeance are negligible in that case. However, for stronger fluctuating pores — and, hence, more compressible liquids — the discussed effects are expected to be more pronounced.

Flow enhancement in compliant nanopores. Our simulation data allow us to quantify the effect of the compliance of a nanoporous material on the resulting permeance according to Eq. (12). In Fig. 6(a), we plot the permeance K as a function of the resulting average pore size $\langle H\rangle$. Comparison of the fluctuating compliant pores with simulations at the same mean pore size and water numbers [filled vs. empty symbols in Fig. 6(a)] shows that fluctuations in the slit nanopore do not enhance transport, also see Fig. 5(b) and in line with the findings discussed in the previous paragraph. Yet, the molecular simulation data show a strong increase of K with decreasing stiffness at the same average pore size $\langle H\rangle$. In other words, softer pores lead to transport enhancement due to the pore compliance itself. This is due to the fact that at the same bulk pressure (i.e. chemical potential), due to the different elastic properties of the slit pores, water can accommodate in different density profiles, and thus

a larger net amount of water is present that can be transported, c.f. Figs. 1 and 2. These thermodynamic effects that change the water density profile and viscosity close to the surface seem to be the main driving parameter leading to flow properties (Fig. 4).

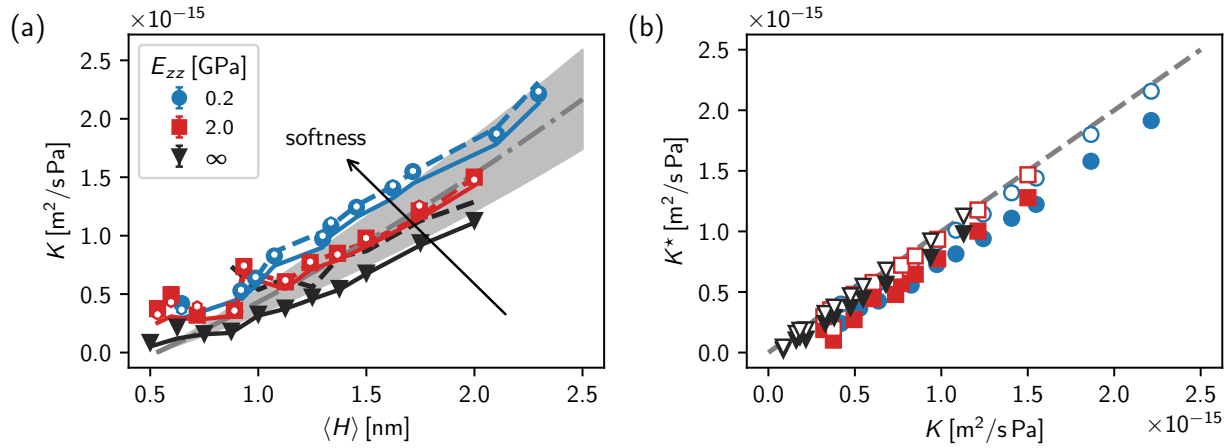

FIG. 6: **Permeance.** The permeance K is shown as a function of pore size $\langle H \rangle$ for the soft (blue circles), stiff (red squares), and rigid pores (black triangles). Filled and empty symbols denote simulation data evaluated according to Eq. (12) for the fluctuating and frozen pores, respectively. The gray dashed-dotted line denotes the expected permeance from Poiseuille equation Eq. (10) if a homogeneous density profile, bulk viscosity, and a slip length of $1.2 \pm 0.3\,\mathrm{nm}$ are assumed (see Figure S5 in the Supplementary Information). Shaded area denotes the corresponding uncertainty in the extrapolated slip length. Colored dashed lines further take into account the fitted slip lengths for each pore height and stiffness, data $H < 1\,\mathrm{nm}$ are excluded due to their large uncertainty, see Figure S5 in the Supplementary Information. Solid lines are constructed from the fitted Poiseuille profiles taking into account the density weighted velocity profiles, Eq. (13). (b) Permeance $K^\star$ calculated according to Eq. (14) vs. the permeance measured directly from the flux in (a). Solid symbols correspond to the classical result of Eq. (2), neglecting the surface excess n_σ, whereas empty symbols take into account the fitted surface excess $n_\sigma = -8.6\,\mathrm{nm}^{-2}$ obtained in Fig. 2. The dashed line serves as guide to the eye.

The solid lines in Fig. 6(a) show the permeance predicted from the two-zone Poiseuille flow weighted by the water density profile,

$$K = -\frac{\int \rho(z) v(z)\,\mathrm{d}z}{\int \rho(z)\,\mathrm{d}z} \frac{\langle H \rangle A}{N \nabla \mu}. \tag{13}$$

In this equation, the term $(\langle H \rangle A) / (N \nabla \mu) = 1/\nabla P$ again relates chemical potential and pressure gradients as driving force according to a Gibbs–Duhem relation. The simulation

data are excellently described by Eq. (13) with a systematic underestimation of the permeance that increases with increasing softness and pore width. This is due to the limited ability of the two-zone Poiseuille flow model to appropriately describe the profiles, see Figures S3 and S4 in the Supplementary Information. While more sophisticated models for the interfacial viscosity — like e.g. an exponential decay to the interfacial value[37] — can be established, their discussion lies out of scope of the present work and the observed deviations do not change our main conclusions.

Following the idea of a coarse-grained model for the pore flux above, we now assume that a Poiseuille flow with slip, Eq. (10) describes accurately the permeance for $\eta = \eta_\mathrm{b}$ and $b = 1.2 \pm 0.3\,\mathrm{nm}$. The resulting permeance is shown as dashed gray line and corresponding shaded area in Fig. 6(a), revealing an overall good agreement with the simulation data (symbols). However, the applicability of this model is limited by the fact that the extrapolated slip length is subject to rather large uncertainty and is not necessarily the same for the different pore elasticities considered. Indeed, we find that good agreement using the coarse-grained model with the measured permeance for $H \gtrsim 1\,\mathrm{nm}$ when the distance-dependent values of b are determined according to Eq. (8) from fits of the two-zone model as shown in Figure S5 in the Supplementary Information. For smaller pore sizes, the fitting procedure is not robust enough to accurately predict the ratio b/H. Significant deviations in the predicted permeance from this approach are only observed for the pore with infinite stiffness. This is due to the fact that density layering is the strongest for this system, which is included in Eq. (13) and thus shows perfect agreement with the simulation data [solid lines in Fig. 6(a)]. The observations above suggest that for sufficiently large pores the assumption of a homogeneous density and parabolic Poiseuille profile with slip boundary conditions predicts accurately the permeance for nanopores (even though significant interfacial layering and slip effects are present). Note that this conclusion still relies on introducing a hydrodynamic pore size $H^\star = H - 2\sigma$ as discussed above.

Finally, we now link the permeance — which is a macroscopic quantity amenable to

simple experimental testing — to the microscopic quantity D_0. For a homogeneous fluid, one expects Eq. (2) to hold. In Fig. 6(b), we compare the permeance $K^\star$ predicted from Eq. (2) and the collective diffusivity D_0 determined from the simulations (Figure S6 in the Supplementary Information) with the measured permeance K. These data are compared for the different values E_{zz} considered in this work. Eq. (2) strictly underestimates the permeance due to the neglect of the surface excess when assuming a homogeneous, bulk-like density. This can be accounted for by a modified expression,

$$K^\star = D_0 H \frac{1}{k_\mathrm{B}T\left(n_\sigma + \rho_\mathrm{b} H\right)}, \tag{14}$$

in which we use $n_\sigma = -8.6\,\mathrm{nm}^{-2}$ (see discussion above). The corresponding comparison corresponds to the empty symbols in Fig. 6(b). The collapse of the data on the bisector reveals that Eq. (14) allows for a consistent link between K and D_0 through the concepts of interfacial thermodynamics (including the significant surface layering which leads to strong fluctuations with respect to a simple homogeneous density profile). The latter finding thus paves the way to consistent interpretation of microscopic dynamics — incorporated in D_0 and measured experimentally typically in scattering experiments — to the permeance K, that is accessible from experimental hydraulic flow measurements through a porous material.

In conclusion, whereas the compliance of a nanoporous material strongly influences the transport in deformable nanopores due to the different density layering and, thus, different interfacial viscous effects, pore size fluctuations do not enhance the flow in the system considered here. While permeance enhancement is expected from a theoretical viewpoint, the absence of such poromechanical effect is due to the large pores and/or fluid incompressibility involved in our systems. We note, however, that for smaller pores and more flexible materials these effects could become highly relevant and encanced transport due to the compliant material appears. More importantly, we find that a consistent pore size definition can be employed to relate accurately the thermodynamics and transport of the nanoconfined fluid.

In particular, when invoking the Gibbs dividing surface, we find that the classical description through a Poiseuille flow holds perfectly at the nanoscale. Active driving of fluctuating membranes has been suggested to increase selectivity and transport,[65] whereas additional effects appear through the phonon-fluid coupling.[16] Thus, it is promising to further explore flow and selectivity manipulation for stronger fluctuating systems in future work. In this context, by providing a consistent description to account for transport and thermodynamics of fluids confined in nanoporous materials, we believe that the present work offers a robust framework for such perspectives.

Methods

GCMC/MD Simulations

All molecular simulation results were obtained using the Large-scale Atomic/Molecular Massively Parallel Simulator (LAMMPS) version 30 Oct 2019.[66] Water is treated using the SPC/E model[67] kept rigid via the SHAKE algorithm[68] and the slit pore was constructed as described in Section II of the Supplementary Information. Input files are freely available in the data repository of the University of Stuttgart (DaRUS).[69] In the molecular simulations, the carbon, oxygen and hydrogen atoms of the host matrix were treated as Lennard-Jones particles with previously established parameters that well account for experimental adsorption isotherms,[40,70,71] see Table S1 in the Supporting Information. All molecular simulations were run at temperature $T = 300\,\mathrm{K}$ using a Nosé-Hoover thermostat[72] with a characteristic damping time of 0.2 ps. The integration timestep of 2 fs was used. Short-range interactions were cutoff and shifted to zero at 9 Å and long-range electrostatics was treated using the PPPM method[73] with an accuracy of 10^{-4}. For the slab system, we additionally used the correction by Yeh and Berkowitz[74] with a total vacuum layer of 3 times the slab separation.

During the GCMC/MD simulations, we performed every 1 ps 2×10^4 insertion/deletion steps for water molecules in the slab. To obtain convergence, typical 10^6 GCMC steps/water molecule were employed, which corresponds to a total simulation time of about 10 ns per

system to sample the equilibrium particle number. The water chemical potential was converted into a corresponding reservoir pressure using independent simulations of bulk water, as explained in Section III of the Supplementary Information. The value $\mu = -11.4\,\mathrm{kcal/mol}$ used here was thus found to correspond to an external pressure of $P_0 = 215\,\mathrm{bar}$. This value is sufficient for the pores to always be filled within the range of values σ_{zz}, H_0 reported in Fig. 2.

Equilibrium MD Simulations

To setup equilibrium MD simulations, slit pores with the average number N_w as determined above were constructed. All other simulation parameters were left unchanged. Systems were equilibrated for 1 ns and then productions runs of 250 ns length were performed during which the unfolded coordinates were recorded every 1 ps to calculate the mean-squared displacement. The latter were used to infer the collective and self diffusivities as $D_0 = \lim_{t\to\infty} 1/(2N_\mathrm{w}dt)\langle\sum_{i,j}\left[\mathbf{r}_i(t)-\mathbf{r}_i(0)\right]\cdot\left[\mathbf{r}_j(t)-\mathbf{r}_j(0)\right]\rangle$ and $D_\mathrm{s} = \lim_{t\to\infty} 1/(2dt)\langle|\mathbf{r}(t)-\mathbf{r}(0)|^2\rangle$, respectively. In these equations, $d = 2$ is the dimensionality of the slit pore and the corresponding displacement $\mathbf{r}$ is calculated in the planar directions only. Typical curves for the mean-squared displacement are shown in Figure S7 in the Supplementary Information. Care has to be taken in the determination of the diffusion coefficients from the mean-squared displacement since on the one hand the limit $t \to \infty$ has to be approximated, but on the other hand the statistics gets very poor for large t (see Figure S7 in the Supplementary Information). In practice, to reliably determine a reasonable fitting range, we determine the time-dependent values $D_0(t) = 1/(2N_\mathrm{w}dt)\langle\sum_{i,j}\left[\mathbf{r}_i(t)-\mathbf{r}_i(0)\right]\cdot\left[\mathbf{r}_j(t)-\mathbf{r}_j(0)\right]\rangle$ and $D_\mathrm{s}(t) = 1/(2dt)\langle|\mathbf{r}(t)-\mathbf{r}(0)|^2\rangle$, shown in Figure S7 in the Supplementary Information, and average the data over the range where it is roughly constant, i.e. typically between 250-5000 ps to evaluate D_s and 100-1000 ps to evaluate D_0 for all systems except the smallest pores, where the plateau is observed even for smaller time intervals only due to the small values of the diffusion coefficients.

Alternatively, the diffusion constant can be determined from the velocity autocorrelation functions, $D_0 = 1/(N_\mathrm{w} d) \int_0^\infty \langle \sum_{i,j} \mathbf{v}_i(t) \cdot \mathbf{v}_j(0) \rangle$ and $D_\mathrm{s} = 1/d \int_0^\infty \langle \mathbf{v}(t) \cdot \mathbf{v}(0) \rangle$. Note that the velocity correlation function of water is dominated by the femtosecond timescale as shown in Figure S8 in the Supplementary Information, thus requiring a high dump frequency for the velocities. In practice, we recorded the velocities every timestep and after 1 ns the correlation function was evaluated via fast Fourier transformation using the convolution theorem. The resulting correlation functions are averaged over the total simulation time and finally integration is performed. The limit $t \to \infty$ needs to be replaced by some appropriate fitting range to obtain the extrapolation as shown in Figure S8 in the Supplementary Information. As also shown therein, both approaches give – as expected – results that are in perfect agreement. However, D_s involves an average over all N_w water molecules whereas D_0 corresponds to the water's center of mass movement. Therefore, significantly less statistics is used to measure D_0.

Non-equilibrium MD Simulations

Non-equilibrium simulations were performed by applying a constant force $f_x = -\Delta\mu/L_x$ on all water oxygen atoms along the x-direction. This driving force corresponds to a chemical potential difference $\Delta\mu$ over the corresponding length L_x of the simulation box. We made sure that the resulting mean velocity and permeance remained within the linear response regime, cf. Fig. 3. To avoid any coupling between the applied force and the system thermalization, only the y and z components of the velocity were considered for calculating the thermal energy. All other simulation parameters were the same as explained above. After an initial equilibration of 1 ns, molecular simulations were performed for a total length of 500 ns per system during which positions and velocities were recorded every 10 ps.

Data analysis

All obtained simulation data were analyzed using MDAnalysis[75] and our in-house open source framework MAICoS, https://www.maicos-analysis.org/. Analysis scripts are freely available on the data repository of the University of Stuttgart DaRUS, https://doi.org/10.18419/darus-3966.[69]

Associated content

Supporting Information

The Supporting Information is available free of charge on the publisher's website.

Table S1 and Figures S1-S8, details on the construction of the slit pore, SPC/E bulk water equation of state for the employed simulation setup, diffusion coefficient in bulk water and analysis of pore size and particle number fluctuations.

Author Information

Author Contributions

AS and BC designed the research project; AS performed the simulations; AS and BC analyzed the simulation data; all authors were involved in preparing the manuscript.

Notes

The authors declare no competing financial interest.

Acknowledgments

We acknowledge funding from the Agence Nationale de la Recherche (Project TWIST No. ANR-17-CE08- 0003) and computation time on the GRICAD infrastructure supported by the Equip@Meso project (No. ANR-10-EQPX-29-01). AS acknowledges funding from the DFG under Germany's Excellence Strategy - EXC 2075 – 390740016 and SFB 1313 (Project Number 327154368) and support by the Stuttgart Center for Simulation Science (SimTech).

References

(1) Schoch, R. B.; Han, J.; Renaud, P. Transport Phenomena in Nanofluidics. *Rev. Mod. Phys.* **2008**, *80*, 839–883.

(2) Bocquet, L.; Charlaix, E. Nanofluidics, from Bulk to Interfaces. *Chem. Soc. Rev.* **2010**, *39*, 1073–1095.

(3) Kavokine, N.; Netz, R. R.; Bocquet, L. Fluids at the Nanoscale: From Continuum to Subcontinuum Transport. *Annual Review of Fluid Mechanics* **2021**, *53*, null.

(4) Bazant, M. Z.; Storey, B. D.; Kornyshev, A. A. Double Layer in Ionic Liquids: Overscreening versus Crowding. *Phys. Rev. Lett.* **2011**, *106*, 046102.

(5) Lainé, A.; Niguès, A.; Bocquet, L.; Siria, A. Nanotribology of Ionic Liquids: Transition to Yielding Response in Nanometric Confinement with Metallic Surfaces. *Phys. Rev. X* **2020**, *10*, 011068.

(6) Polster, J. W.; Souna, A. J.; Motevaselian, M. H.; Lucas, R. A.; Tran, J. D.; Siwy, Z. S.; Aluru, N. R.; Fourkas, J. T. The Electrical-Double Layer Revisited. *Natural Sciences n/a*, e20210099.

(7) Coppens, M.-O. A Nature-Inspired Approach to Reactor and Catalysis Engineering. *Current Opinion in Chemical Engineering* **2012**, *1*, 281–289.

(8) Yang, H. Y.; Han, Z. J.; Yu, S. F.; Pey, K. L.; Ostrikov, K.; Karnik, R. Carbon Nanotube Membranes with Ultrahigh Specific Adsorption Capacity for Water Desalination and Purification. *Nat Commun* **2013**, *4*, 2220.

(9) Shao, H.; Wu, Y.-C.; Lin, Z.; Taberna, P.-L.; Simon, P. Nanoporous Carbon for Electrochemical Capacitive Energy Storage. *Chem. Soc. Rev.* **2020**,

(10) Eijkel, J. C. T.; van den Berg, A. Nanofluidics: What Is It and What Can We Expect from It? *Microfluid Nanofluid* **2005**, *1*, 249–267.

(11) Huber, P. Soft Matter in Hard Confinement: Phase Transition Thermodynamics, Structure, Texture, Diffusion and Flow in Nanoporous Media. *J. Phys.: Condens. Matter* **2015**, *27*, 103102.

(12) Ma, M.; Grey, F.; Shen, L.; Urbakh, M.; Wu, S.; Liu, J. Z.; Liu, Y.; Zheng, Q. Water Transport inside Carbon Nanotubes Mediated by Phonon-Induced Oscillating Friction. *Nature Nanotech* **2015**, *10*, 692–695.

(13) Bocquet, L.; Netz, R. R. Phonon Modes for Faster Flow. *Nature Nanotech* **2015**, *10*, 657–658.

(14) Marbach, S.; Dean, D. S.; Bocquet, L. Transport and Dispersion across Wiggling Nanopores. *Nature Phys* **2018**, *14*, 1108–1113.

(15) Marcotte, A.; Mouterde, T.; Niguès, A.; Siria, A.; Bocquet, L. Mechanically Activated Ionic Transport across Single-Digit Carbon Nanotubes. *Nat Mater* **2020**, *19*, 1057–1061.

(16) Noh, Y.; Aluru, N. R. Phonon-Fluid Coupling Enhanced Water Desalination in Flexible Two-Dimensional Porous Membranes. *Nano Lett.* **2022**, *22*, 419–425.

(17) Wei, M.; Liu, Y.; Liu, J.; Elsworth, D.; Zhou, F. Micro-Scale Investigation on Coupling

of Gas Diffusion and Mechanical Deformation of Shale. *Journal of Petroleum Science and Engineering* **2019**, *175*, 961–970.

(18) Berthonneau, J.; Obliger, A.; Valdenaire, P.-L.; Grauby, O.; Ferry, D.; Chaudanson, D.; Levitz, P.; Kim, J. J.; Ulm, F.-J.; Pellenq, R. J.-M. Mesoscale Structure, Mechanics, and Transport Properties of Source Rocks' Organic Pore Networks. *Proceedings of the National Academy of Sciences* **2018**, *115*, 12365–12370.

(19) Hoseini, M.; Bindiganavile, V.; Banthia, N. The Effect of Mechanical Stress on Permeability of Concrete: A Review. *Cement and Concrete Composites* **2009**, *31*, 213–220.

(20) Zhang, Y.; Wan, X.; Hou, D.; Zhao, T.; Cui, Y. The Effect of Mechanical Load on Transport Property and Pore Structure of Alkali-Activated Slag Concrete. *Construction and Building Materials* **2018**, *189*, 397–408.

(21) Bai, M.; Elsworth, D. *Coupled Processes in Subsurface Deformation, Flow, and Transport*; American Society of Civil Engineers, 2000.

(22) Cox, C. D.; Bavi, N.; Martinac, B. Biophysical Principles of Ion-Channel-Mediated Mechanosensory Transduction. *Cell Reports* **2019**, *29*, 1–12.

(23) Darcy, H. *Les fontaines publiques de la ville de Dijon: Exposition et application des principes à suivre et des formules à employer dans les questions de distribution d'eau : Ouvrage terminé par un appendice relatif aux fournitures d'eau de plusieurs villes, au filtrage des eaux et à la fabrication des tuyaux de fonte, de plomb, de tôle et de bitume*; Victor Dalmont, éditeur, 1856.

(24) Whitaker, S. Flow in Porous Media I: A Theoretical Derivation of Darcy's Law. *Transp Porous Med* **1986**, *1*, 3–25.

(25) O'Sullivan, C.; Arson, C.; Coasne, B. A Perspective on Darcy's Law across the Scales:

From Physical Foundations to Particulate Mechanics. *Journal of Engineering Mechanics* **2022**, *148*, 04022064.

(26) Muskat, M. *The Flow of Homogeneous Fluids Through Porous Media*; McGraw-Hill Book Company, Incorporated, 1937.

(27) Thompson, A. P.; Ford, D. M.; Heffelfinger, G. S. Direct Molecular Simulation of Gradient-Driven Diffusion. *J. Chem. Phys.* **1998**, *109*, 6406–6414.

(28) Arya, G.; Chang, H.-C.; Maginn, E. J. A Critical Comparison of Equilibrium, Non-Equilibrium and Boundary-Driven Molecular Dynamics Techniques for Studying Transport in Microporous Materials. *J. Chem. Phys.* **2001**, *115*, 8112–8124.

(29) Bhatia, S. K.; Nicholson, D. Modeling Mixture Transport at the Nanoscale: Departure from Existing Paradigms. *Phys. Rev. Lett.* **2008**, *100*, 236103.

(30) Martin, M. G.; Thompson, A. P.; Nenoff, T. M. Effect of Pressure, Membrane Thickness, and Placement of Control Volumes on the Flux of Methane through Thin Silicalite Membranes: A Dual Control Volume Grand Canonical Molecular Dynamics Study. *J. Chem. Phys.* **2001**, *114*, 7174–7181.

(31) Onsager, L. Reciprocal Relations in Irreversible Processes. I. *Phys. Rev.* **1931**, *37*, 405–426.

(32) Bhatia, S. K.; Bonilla, M. R.; Nicholson, D. Molecular Transport in Nanopores: A Theoretical Perspective. *Phys. Chem. Chem. Phys.* **2011**, *13*, 15350–15383.

(33) Falk, K.; Coasne, B.; Pellenq, R.; Ulm, F.-J.; Bocquet, L. Subcontinuum Mass Transport of Condensed Hydrocarbons in Nanoporous Media. *Nature Communications* **2015**, *6*, 6949.

(34) Obliger, A.; Pellenq, R.; Ulm, F.-J.; Coasne, B. Free Volume Theory of Hydrocarbon Mixture Transport in Nanoporous Materials. *J. Phys. Chem. Lett.* **2016**, *7*, 3712–3717.

(35) Sastre, G.; Kärger, J.; Ruthven, D. M. Molecular Dynamics Study of Diffusion and Surface Permeation of Benzene in Silicalite. *J. Phys. Chem. C* **2018**, *122*, 7217–7225.

(36) Bukowski, B. C.; Keil, F. J.; Ravikovitch, P. I.; Sastre, G.; Snurr, R. Q.; Coppens, M.-O. Connecting Theory and Simulation with Experiment for the Study of Diffusion in Nanoporous Solids. *Adsorption* **2021**, *27*, 683–760.

(37) Schlaich, A.; Kappler, J.; Netz, R. R. Hydration Friction in Nanoconfinement: From Bulk via Interfacial to Dry Friction. *Nano Lett.* **2017**, *17*, 5969–5976.

(38) Chakraborty, S.; Kumar, H.; Dasgupta, C.; Maiti, P. K. Confined Water: Structure, Dynamics, and Thermodynamics. *Acc. Chem. Res.* **2017**, *50*, 2139–2146.

(39) Tinti, A.; Camisasca, G.; Giacomello, A. Structure and Dynamics of Water Confined in Cylindrical Nanopores with Varying Hydrophobicity. *Philosophical Transactions of the Royal Society A: Mathematical, Physical and Engineering Sciences* **2021**, *379*, 20200403.

(40) Bousige, C.; Ghimbeu, C. M.; Vix-Guterl, C.; Pomerantz, A. E.; Suleimenova, A.; Vaughan, G.; Garbarino, G.; Feygenson, M.; Wildgruber, C.; Ulm, F.-J.; Pellenq, R. J.-M.; Coasne, B. Realistic Molecular Model of Kerogen's Nanostructure. *Nature Materials* **2016**, *15*, 576–582.

(41) Israelachvili, J. N.; Pashley, R. M. Molecular Layering of Water at Surfaces and Origin of Repulsive Hydration Forces. *Nature* **1983**, *306*, 249–250.

(42) Hayashi, T.; Pertsin, A. J.; Grunze, M. Grand Canonical Monte Carlo Simulation of Hydration Forces between Nonorienting and Orienting Structureless Walls. *The Journal of Chemical Physics* **2002**, *117*, 6271–6280.

(43) Li, T.-D.; Gao, J.; Szoszkiewicz, R.; Landman, U.; Riedo, E. Structured and Viscous Water in Subnanometer Gaps. *Phys. Rev. B* **2007**, *75*, 115415.

(44) Chattoraj, D. K.; Birdi, K. S. *Adsorption and the Gibbs Surface Excess*; Plenum Press: New York, 1984.

(45) Ismail, A. F.; Khulbe, K. C.; Matsuura, T. *Gas Separation Membranes: Polymeric and Inorganic*, 2015th ed.; Springer: Cham Heidelberg New York Dordrecht London, 2015.

(46) Brochard, L.; Vandamme, M.; Pellenq, R. J. M. Poromechanics of Microporous Media. *Journal of the Mechanics and Physics of Solids* **2012**, *60*, 606–622.

(47) Gor, G. Y.; Huber, P.; Bernstein, N. Adsorption-Induced Deformation of Nanoporous Materials—A Review. *Applied Physics Reviews* **2017**, *4*, 011303.

(48) Kolesnikov, A. L.; Budkov, Y. A.; Gor, G. Y. Models of Adsorption-Induced Deformation: Ordered Materials and Beyond. *J. Phys.: Condens. Matter* **2021**, *34*, 063002.

(49) Motakabbir, K. A.; Berkowitz, M. Isothermal Compressibility of SPC/E Water. *J. Phys. Chem.* **1990**, *94*, 8359–8362.

(50) Eskandari-Ghadi, M.; Zhang, Y. Mechanics of Shrinkage-Swelling Transition of Microporous Materials at the Initial Stage of Adsorption. *International Journal of Solids and Structures* **2021**, *222–223*, 111041.

(51) Kanduč, M.; Schlaich, A.; Schneck, E.; Netz, R. R. Water-Mediated Interactions between Hydrophilic and Hydrophobic Surfaces. *Langmuir* **2016**, *32*, 8767–8782.

(52) Erbaş, A.; Horinek, D.; Netz, R. R. Viscous Friction of Hydrogen-Bonded Matter. *J. Am. Chem. Soc.* **2012**, *134*, 623–630.

(53) Hansen, J.-P.; McDonald, I. R. *Theory of Simple Liquids: With Applications to Soft Matter*; Academic Press, 2013.

(54) Kärger, J.; Ruthven, D. M.; Theodorou, D. N. *Diffusion in Nanoporous Materials*; John Wiley & Sons, 2012.

(55) Boţan, A.; Rotenberg, B.; Marry, V.; Turq, P.; Noetinger, B. Hydrodynamics in Clay Nanopores. *J. Phys. Chem. C* **2011**, *115*, 16109–16115.

(56) Bocquet, L.; Barrat, J.-L. Hydrodynamic Boundary Conditions, Correlation Functions, and Kubo Relations for Confined Fluids. *Phys. Rev. E* **1994**, *49*, 3079–3092.

(57) Herrero, C.; Omori, T.; Yamaguchi, Y.; Joly, L. Shear Force Measurement of the Hydrodynamic Wall Position in Molecular Dynamics. *J. Chem. Phys.* **2019**, *151*, 041103.

(58) Sokhan, V. P.; Nicholson, D.; Quirke, N. Fluid Flow in Nanopores: Accurate Boundary Conditions for Carbon Nanotubes. *The Journal of Chemical Physics* **2002**, *117*, 8531–8539.

(59) Geng, X.; Yu, M.; Zhang, W.; Liu, Q.; Yu, X.; Lu, Y. Slip Length and Structure of Liquid Water Flowing Past Atomistic Smooth Charged Walls. *Sci Rep* **2019**, *9*, 18957.

(60) Vo, T. Q.; Kim, B. Transport Phenomena of Water in Molecular Fluidic Channels. *Sci Rep* **2016**, *6*, 33881.

(61) Ma, L.; Gaisinskaya-Kipnis, A.; Kampf, N.; Klein, J. Origins of Hydration Lubrication. *Nature Communications* **2015**, *6*, 6060.

(62) Leng, Y.; Cummings, P. T. Fluidity of Hydration Layers Nanoconfined between Mica Surfaces. *Phys. Rev. Lett.* **2005**, *94*, 026101.

(63) Shaat, M.; Javed, U.; Faroughi, S. Wettability and Confinement Size Effects on Stability of Water Conveying Nanotubes. *Sci Rep* **2020**, *10*, 17167.

(64) Köhler, M. H.; da Silva, L. B. Size Effects and the Role of Density on the Viscosity of Water Confined in Carbon Nanotubes. *Chemical Physics Letters* **2016**, *645*, 38–41.

(65) Marbach, S.; Bocquet, L. Active Sieving across Driven Nanopores for Tunable Selectivity. *The Journal of Chemical Physics* **2017**, *147*, 154701.

(66) Plimpton, S. Fast Parallel Algorithms for Short-Range Molecular Dynamics. *J. Comput. Phys.* **1995**, *117*, 1–19.

(67) Berendsen, H. J. C.; Grigera, J. R.; Straatsma, T. P. The Missing Term in Effective Pair Potentials. *J. Phys. Chem.* **1987**, *91*, 6269–6271.

(68) Ryckaert, J.-P.; Ciccotti, G.; Berendsen, H. J. C. Numerical Integration of the Cartesian Equations of Motion of a System with Constraints: Molecular Dynamics of n-Alkanes. *Journal of Computational Physics* **1977**, *23*, 327–341.

(69) Schlaich, A. Replication Data for: Bridging Microscopic Dynamics and Hydraulic Permeability in Mechanically-Deformed Nanoporous Materials. 2024; https://doi.org/10.18419/darus-3966.

(70) Billemont, P.; Coasne, B.; De Weireld, G. Adsorption of Carbon Dioxide, Methane, and Their Mixtures in Porous Carbons: Effect of Surface Chemistry, Water Content, and Pore Disorder. *Langmuir* **2013**, *29*, 3328–3338.

(71) Pikunic, J.; Clinard, C.; Cohaut, N.; Gubbins, K. E.; Guet, J.-M.; Pellenq, R. J.-M.; Rannou, I.; Rouzaud, J.-N. Structural Modeling of Porous Carbons: Constrained Reverse Monte Carlo Method. *Langmuir* **2003**, *19*, 8565–8582.

(72) Shinoda, W.; Shiga, M.; Mikami, M. Rapid Estimation of Elastic Constants by Molecular Dynamics Simulation under Constant Stress. *Phys. Rev. B* **2004**, *69*, 134103.

(73) Plimpton, S.; Pollock, R.; Stevens, M. Particle-Mesh Ewald and rRESPA for Parallel Molecular Dynamics Simulations. In Proceedings of the Eighth SIAM Conference on Parallel Processing for Scientific Computing. 1997.

(74) Yeh, I.-C.; Berkowitz, M. L. Ewald Summation for Systems with Slab Geometry. *The Journal of Chemical Physics* **1999**, *111*, 3155–3162.

(75) Michaud-Agrawal, N.; Denning, E. J.; Woolf, T. B.; Beckstein, O. MDAnalysis: A Toolkit for the Analysis of Molecular Dynamics Simulations. *J. Comput. Chem.* **2011**, *32*, 2319–2327.

SUPPORTING INFORMATION for: Bridging Microscopic Dynamics and Hydraulic Permeability in Mechanically-Deformed Nanoporous Materials

Alexander Schlaich,[1,2,3,*] Matthieu Vandamme,[4] Marie Plazanet,[3] and Benoit Coasne[3,5,†]

[1] *Stuttgart Center for Simulation Science (SC SimTech), University of Stuttgart, 70569 Stuttgart, Germany*

[2] *Institute for Computational Physics, University of Stuttgart, 70569 Stuttgart, Germany*

[3] *Univ. Grenoble Alpes, CNRS, LIPhy, 38000 Grenoble, France*

[4] *Navier, Ecole des Ponts, Univ. Gustave Eiffel, CNRS, Marne-la-Vallée, France*

[5] *Institut Laue Langevin, F-38042 Grenoble, France*

(Dated: March 28, 2024)

CONTENTS

I. Supplementary Figures and Tables 1

II. Construction of the slit pore 8

III. Bulk water equation of state 9

IV. Diffusion coefficient in bulk water 10

References 11

I. SUPPLEMENTARY FIGURES AND TABLES

	CC	OO	HH
σ [Å]	3.4	3.0	2.42
ϵ [K]	28.0	85.6	15.1

Table S1. Carbon, oxygen, and hydrogen Lennard-Jones parameters used in the GCMC and MD simulations for the slit pore. The cross interactions with water are computed from the Lorentz-Berthelot rules.

* alexander.schlaich@simtech.uni-stuttgart.de
† benoit.coasne@univ-grenoble-alpes.fr

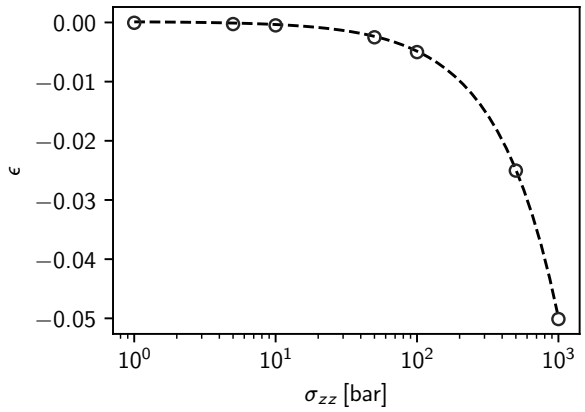

FIG. S1. **Hookean behavior of the empty compliant pore.** Normal stress σ_{zz} vs. strain $\epsilon = (l - l_0)/(l_0)$. Symbols denote simulation data for an empty pore, $H = 1\,\mathrm{nm}$ and modulus $E_{zz} = 2\,\mathrm{GPa}$. Dashed line shows the linear behavior, $\epsilon = -\sigma/E$.

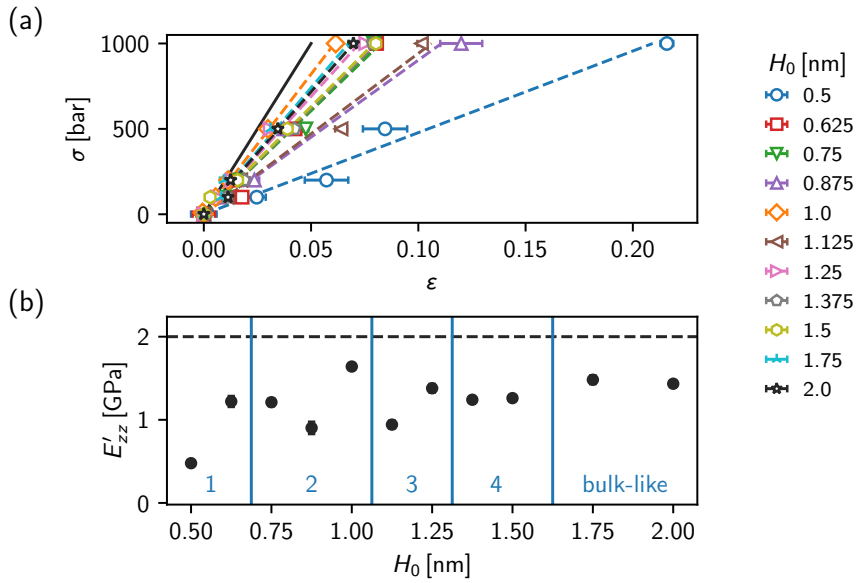

FIG. S2. **Analysis of the effective pore modulus for the stiffer pore, $E_{zz} = 2\,\mathrm{GPa}$.** (a) Stress-strain relation for stiff pores, $E_{zz} = 2\,\mathrm{GPa}$, with different equilibrium pore size H_0 as indicated by the legend on the right. Dashed lines denote fits of the effective modulus according to $\sigma_{zz} = \varepsilon E_{zz}^{(\mathrm{eff})}$. The solid line denotes the empty pore mechanical response without any effect due adsorbed water, $\sigma_{zz} = \varepsilon E_{zz}$. (b) Effective modulus of the stiff system for different equilibrium pore sizes obtained from the fits in (a). The vertical lines denote the different regimes, where in the density profiles 1-4 water layers can be observed. Above $\sim 1.7\,\mathrm{nm}$ the water in the center of the slab is bulk-like, *cf.* density profiles shown in Figs. S3 and S4.

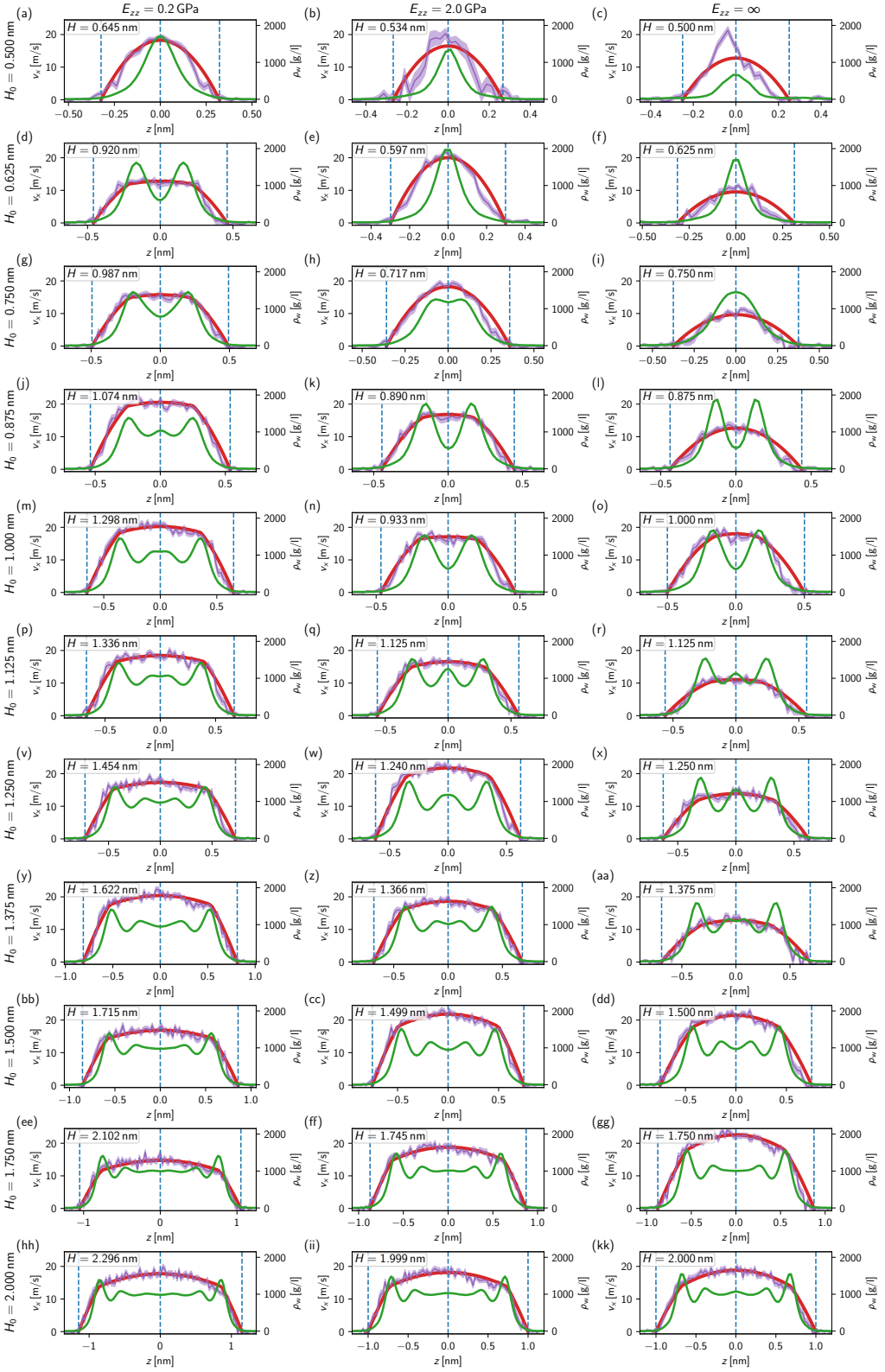

FIG. S3. **Density and velocity profiles for all systems considered.** For the compliant and non-compliant pores we show the density (green) and velocity profiles (purple). Red lines denote fits of the two-zone Poiseuille model to the velocity profiles, see main text. Dashed horizontal lines denote the position of the pore surface and its center, respectively.

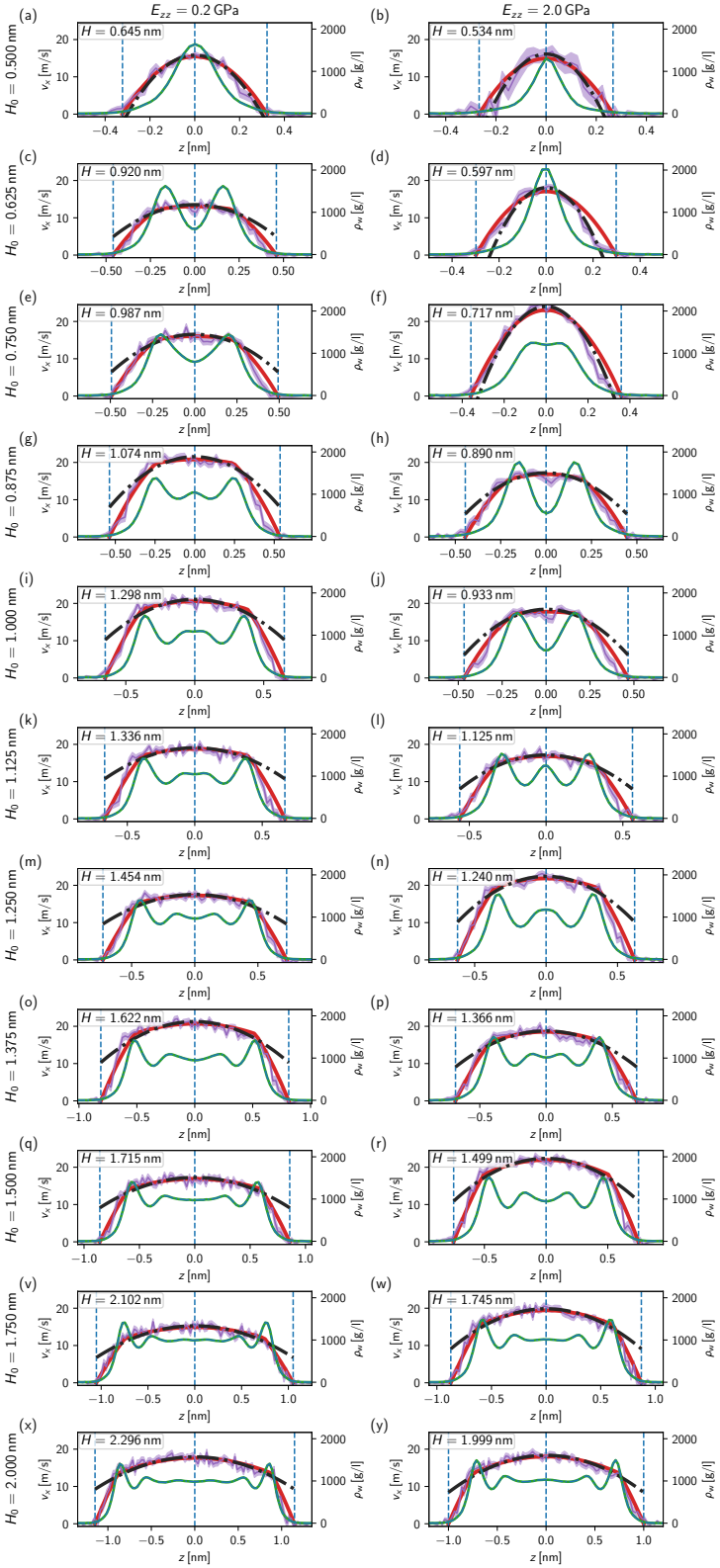

FIG. S4. **Density and velocity profiles the non-fluctuating compliant pores.** As in Fig. S3, the density (green) and velocity profiles (purple) are shown. Red lines denote fits of the two-zone Poiseuille model to the velocity profiles, see main text. Additionally, dahed-dotted black lines indicate the coarse-grained fit of the Poiseuille profile data revealing slip. Dashed horizontal lines denote the position of the pore surface and its center, respectively.

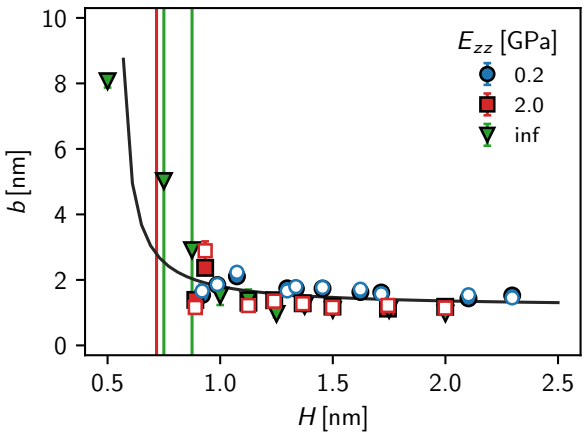

FIG. S5. **Slip length.** Slip lengths according to Eqs. (8) and (9) obtained from the fits of the two-zone Poiseuille flow to the simulation data. The solid line denotes the slip length computed using the values at large distances, $w = \sigma$ and $\bar{\eta}_\mathrm{i}$. The colored vertical lines denote the error bars, revealing that for the small pores this procedure does not allow to reliably extract the slip length. However, these values are well consistent with the expected behavior from the large pore sizes (solid black line).

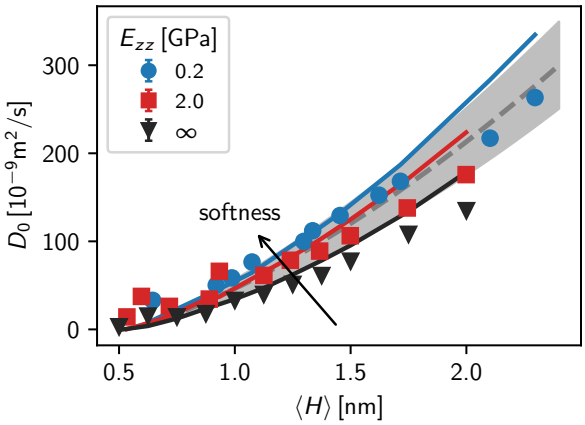

FIG. S6. **Collective diffusion.** The diffusion constant D_0 is shown as a function of pore size H for the soft (circles), stiff (squares), and rigid pores (triangles). Symbols denote simulation results from the non-equilibrium simulations according to the data shown in Fig. 3, whereas the dashed gray lines is showing the classical Poiseuille prediction, Eq. (11) of the main text with $\eta = \eta_\mathrm{b}$ and $b = 1.2 \pm 0.3\,\mathrm{nm}$ (the shaded are corresponds to the uncertainty in the slip length). Colored lines denote data using Eq. (11) of the main text, but with distance-dependent values of the slip length and apparent viscosity (Fig. S5).

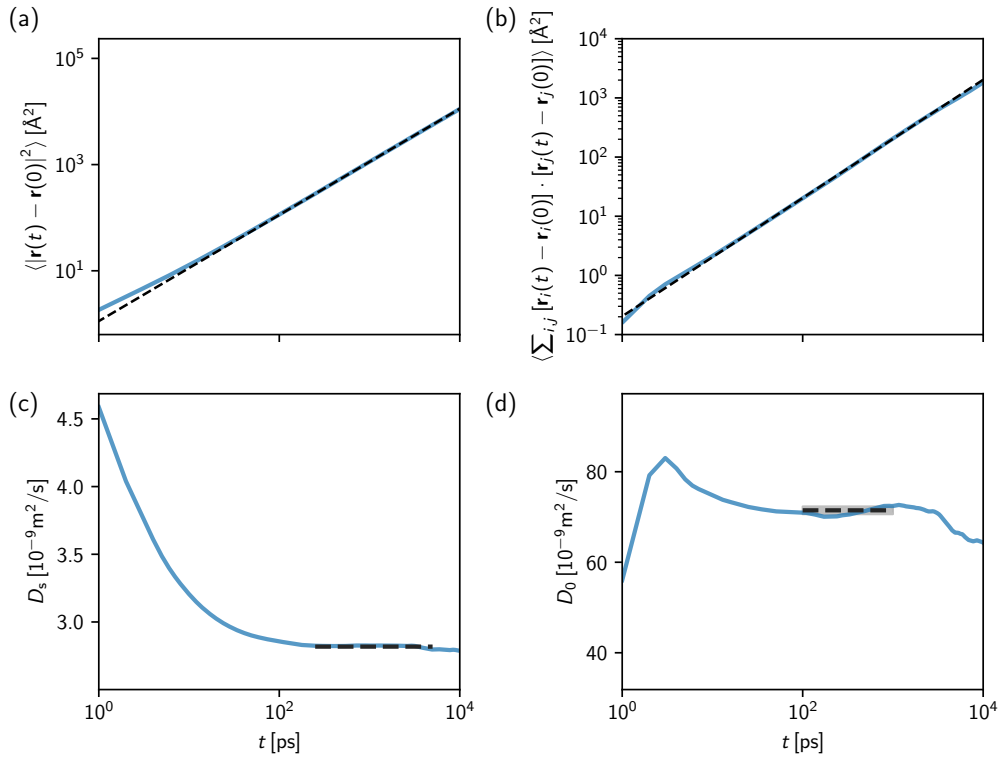

FIG. S7. **Analysis of the mean-squared displacement to obtain self and collective diffusion coefficients.** Data is exemplarily shown for the pore with modulus $E_{zz} = 2\,\mathrm{GPa}$ and height $H = 0.9\,\mathrm{nm}$. Shown in (a) and (b) are the mean-squared displacements (MSD) $\langle|\mathbf{r}(t)-\mathbf{r}(0)|^2\rangle$ and $\langle\sum_{i,j}[\mathbf{r}_i(t)-\mathbf{r}_i(t)]\cdot[\mathbf{r}_j(t)-\mathbf{r}_j(t)]\rangle$, respectively, that correspond to the self and collective diffusion. Instead of determining appropriate fitting ranges from this data, we show in (c) and (d) the corresponding MSD divided by $(2dt)$ yielding directly the diffusion coefficient in the limit $t \to \infty$. The fitting result is shown as dashed horizontal line, the length of which indicates the fitting ranges (between 250-5000 ps for D_s and 100-1000 ps for D_0, respectively). Dashed lines in (a) and (b) denote the MSD according to the fitted diffusion constant.

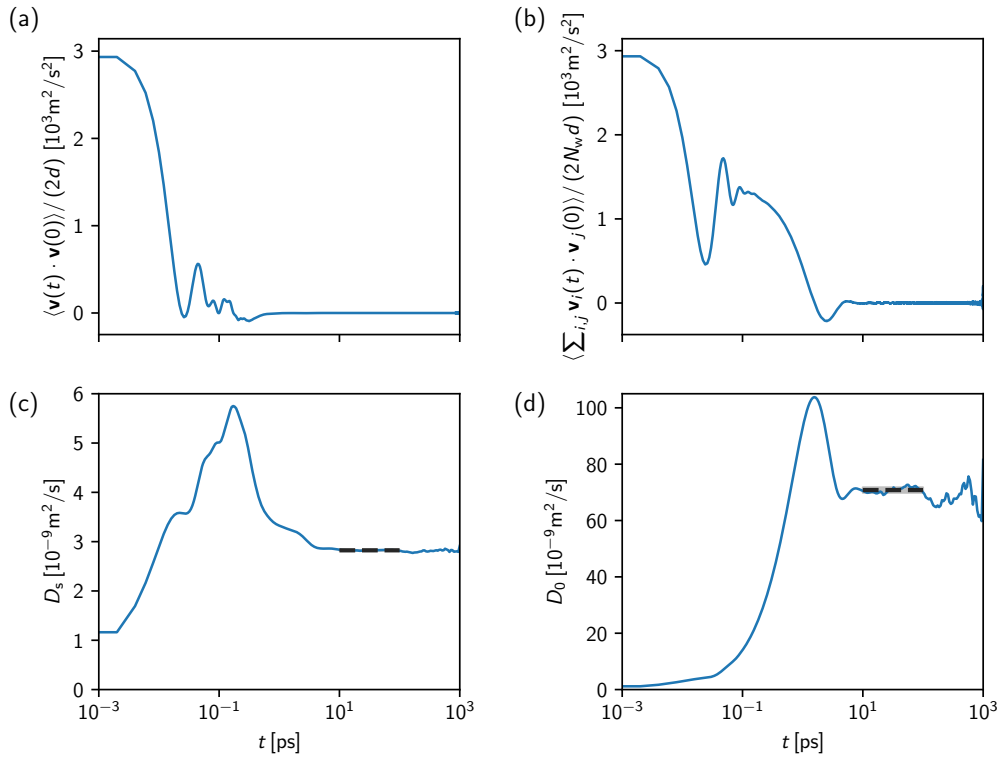

FIG. S8. **Analysis of the velocity auto-correlation function to obtain self and collective diffusion coefficients.** Data is exemplarily shown for the pore with modulus $E_{zz} = 2\,\mathrm{GPa}$ and height $H = 0.9\,\mathrm{nm}$ (as in Fig. S7). Shown in (a) and (b) are the velocity auto-correlation functions for the self and collective diffusivities, respectively. (c) and (d) denote the corresponding values of the integrals $D_0 = 1/(2N_\mathrm{w}dt)\langle\sum_{i,j}[\mathbf{r}_i(t) - \mathbf{r}_i(0)] \cdot [\mathbf{r}_j(t) - \mathbf{r}_j(0)]\rangle$ and $D_\mathrm{s} = 1/(2dt)\langle|\mathbf{r}(t) - \mathbf{r}(0)|^2\rangle$, which converge to the desired values in limit $t \to \infty$. Due to limited sampling of the auto-correlation function noise appears in the integrals, we this take the mean between 10 and 100 ps, indicated as dashed lines, to calculate D_s and D_0.

II. CONSTRUCTION OF THE SLIT PORE

We construct a chemically realistic, disordered material for the slit pore based on a 25 Å^3 sample of mineral-free shungite (PY02), a rather exceptional kerogen type from Russia, that was obtained using a molecular dynamics-hybrid reverse Monte Carlo approach by Bousige and co-workers [1]. This material only has tiny ratios of oxygen and hydrogen atoms compared to carbon atoms and thus is expected to be rather hydrophobic, as desired in our study. We chose a high density of 1.4 g/cm^3 to obtain a nearly water impermeable material.

For this cubic sample we cut out a slice of 10 Å thickness and estimate the average charge on the carbon, hydrogen and oxygen atoms from a 100 ps simulation at $T = 300$ K using the Reax.ff reactive forcefield with charge equilibration [2, 3] and a timestep of 0.5 fs. The sample is then duplicated, rotated by 90° around the z-axis to avoid symmetry and by 180° around the x-axis to cancel z-component of dipole moment and then translated by H in z-direction to create a slab system. To allow for pore fluctuations without interactions with the periodic images in z, a vacuum layer of 40 Å is added. In order to account for this already existing vacuum layer when computing the electrostatic interactions with the Yeh-Berkowitz correction,[4] the slab correction of LAMMPS is used together with another virtual vacuum layer of 1.5 times the box length, resulting in at least 3 times the box length of the vacuum thickness.

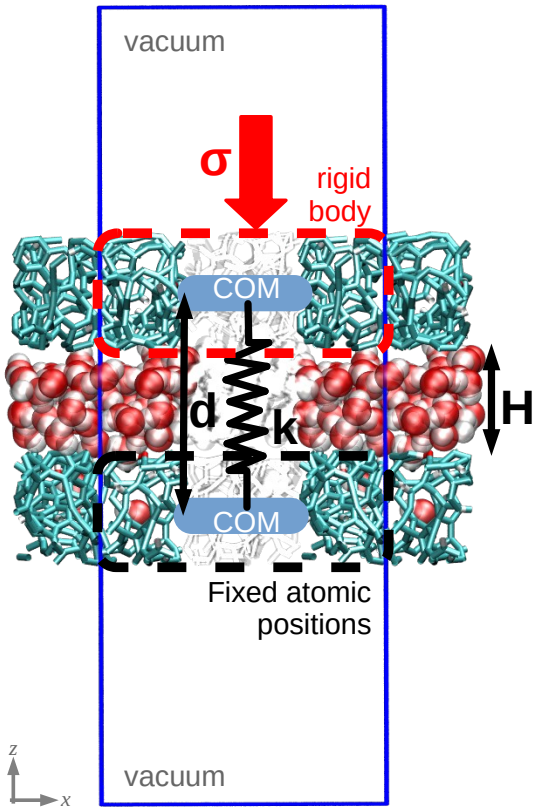

FIG. S9. **Setup of the simulations.** The constructed slit pore is periodic in the xy-plane and separated by a vacuum layer of 4 nm. A Hookean spring of equilibrium length d is acting between the center of mass of the two surfaces resulting in the surface separation H. A stress σ is applied on the fluctuating surface via a homogeneous force density f_z in z-direction.

As explained in the main text, positions of the lower surface (in z-direction) are fixed, whereas the upper surface is allowed to fluctuate. A stress σ_{zz} is applied via a homogeneous force density $f_z = \sigma_{zz} L_x L_y / N_{\text{wall}}$, where $L_x = L_y = 2.5$ nm are the lateral dimensions of the simulation box and $N_{\text{wall}} = 502$ is the number of atoms in one surface. Equations of motion are integrated in the thermalized $N_{\text{water}}VT$ ensemble for water molecules using the Nosé-Hoover thermostat at temperature $T = 300$ K, whereas the fluctuating rigid surface is thermalized only via energy exchange with the water molecules in the $N_{\text{wall}}VE$ ensemble at fluctuating energy E.

III. BULK WATER EQUATION OF STATE

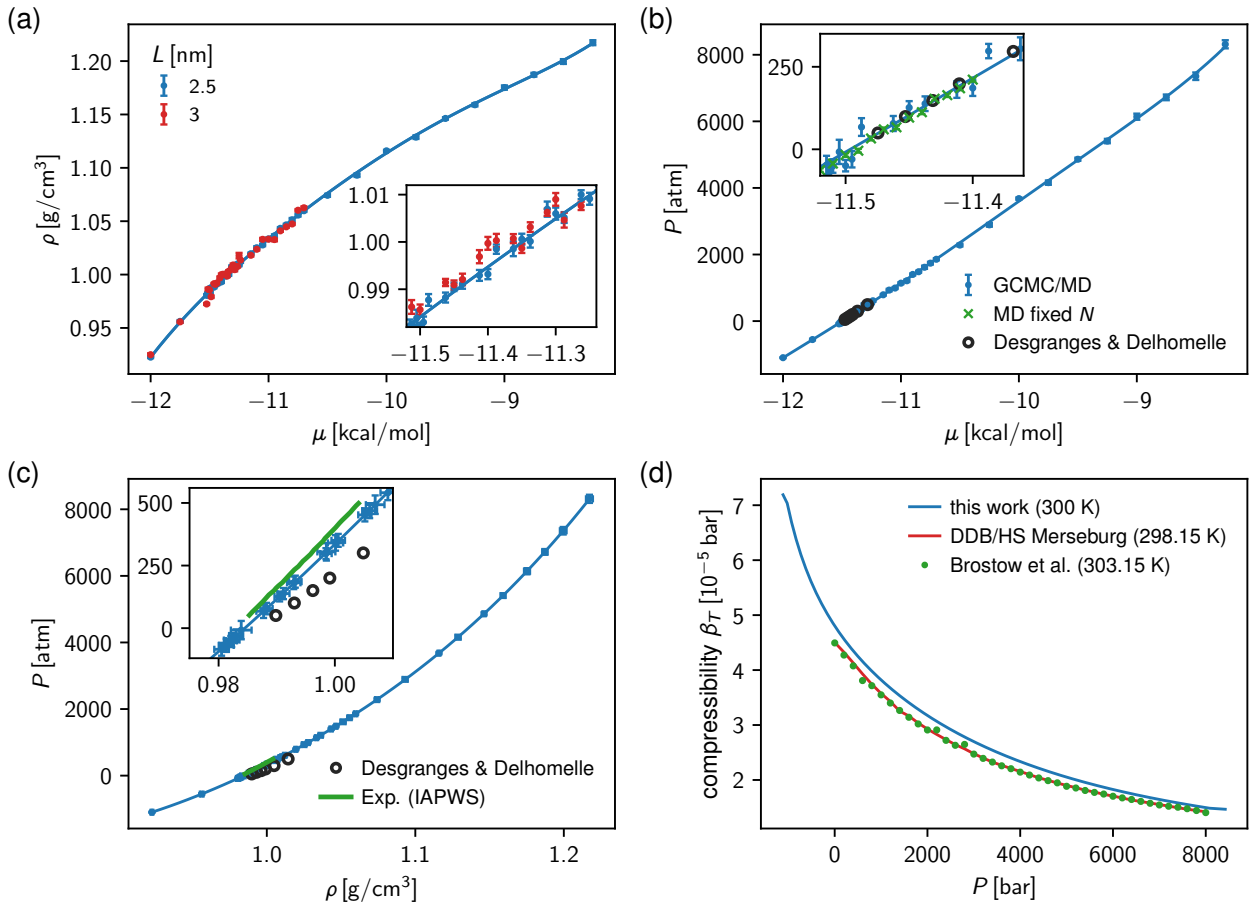

FIG. S10. **GCMC/MD simulations of bulk water in the liquid state.** (a) Density for two box lengths L indicated in the legend and polynomial fit to the data for $L = 2.5\,\mathrm{nm}$. (b) Pressure obtained from the GCMC/MD runs (blue data) and corresponding polynomial fit. Green data show simulation results obtained from MD simulations at fixed particle number $N = \rho L^3$ for the density determined in (a) and $L = 2.5\,\mathrm{nm}$. Empty black circles denote simulation data from Ref.5 obtained in a 2 nm box and using analytical long-range correction for the truncated Lennard-Jones interaction. (c) shows the resulting equation of state together with simulations from Ref.5 and experimental values taken from the IAPWS tables, Ref.6. Isothermal compressibility of SPC/E water using our simulation parameters (blue line) and experimental results from the Dortmund Data Bank, 2022, www.ddbst.com (red line) and Ref.7 recorded at temperatures $T = 298.15\,\mathrm{K}$ and $T = 303.15\,\mathrm{K}$ respectively.

GCMC/MD simulations have been performed for bulk water in a cubic box of box length $L = 2.5\,\mathrm{nm}$ at different values of the chemical potential μ. As for the slab system discussed in the main text every 1 ps a GCMC run of 2×10^4 steps was performed starting from a configuration at typical bulk water density and the total sampling was conducted for 10^6 GCMC steps to obtain convergence with typically 5% of the data being discarded for equilibration; error estimates are obtained by block-averaging the simulation data into 20 independent samples. For the bulk simulations of the SPC/E water kept rigid via the SHAKE algorithm[8] we employ a MD timestep of 2 fs and the Nosé-Hoover thermostat is set to a characteristic damping time of 0.2 ps.[9]

Figure S10(a) shows the resulting density of liquid bulk water for two box lengths $L \in \{2.5, 3\}\,\mathrm{nm}$ to exclude possible finite size effects. The solid line is obtained from a fifth-order polynomial fit to the simulation data. Comparison of the two box lengths reveals no finite size effects. Figure S10(b) shows the corresponding pressure determined from the GCMC/MD run (blue data). Since the fluctuating particle number and the corresponding thermal equilibration of all degrees of freedom within the 1 ps MD run might result in insufficient phase-space sampling we also performed MD simulations at fixed water particle number N_{water} determined from the polynomial fit shown in Fig. S10(a).

The resulting pressures shown as green crosses in Fig. S10(b) perfectly agree with the GCMC/MD data and the corresponding polynomial fit (blue line). We also include in Fig. S10(b) simulation data by Desgranges and Dellhomme obtained via Wang-Landau sampling in a 2 nm cubic simulation box using analytic long-range correction for the truncated Lennard-Jones potential (empty black circles) which perfectly matches our simulation results. From the polynomial fit of the $P-\mu$ relation shown in the inset of Fig. S10(b) we choose the value of the chemical potential employed in the main text, $\mu = -11.4\,\mathrm{kcal/mol}$ which corresponds to target intrusion pressure introduced in the main text, $P_0 = 215\,\mathrm{atm}$.

In Fig. S10(c) we show the water equation of state resulting from our simulations (blue data and blue line denoting a polynomial fit) and experimental results taken from the IAPWS tables,[6] revealing excellent agreement. Interestingly, employing the analytical dispersion correction as in the work by Desgranges and Dellhomme leads to worse results compared to the experimental values for SPC/E water. The polynamial fit in Fig. S10(c) allows to calculate the isothermal compressibility

$$\beta_T = -\frac{1}{v}\frac{\partial v}{\partial P}, \tag{S1}$$

where $v = m_{\mathrm{water}}/\rho$ is the volume of a water molecule and m_{water} is its mass. Comparison of our simulation data at $T = 300\,\mathrm{K}$ [blue line in Fig. S10(d)] with experimental results for β_T at $T = 298.15\,\mathrm{K}$ and $303.15\,\mathrm{K}$, respectively, reveals excellent and near-quantitative agreement for the thermodynamic-mechanical properties and thus justifying the choice of the SPC/E model for this work.

IV. DIFFUSION COEFFICIENT IN BULK WATER

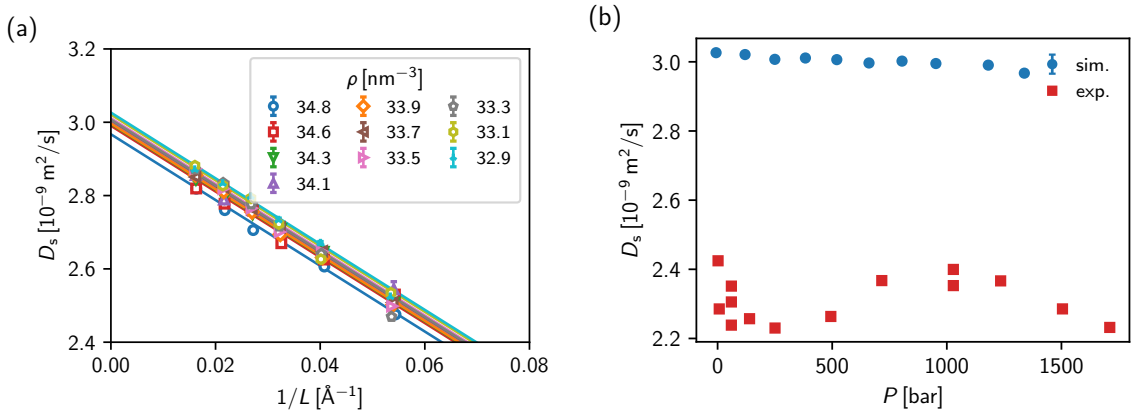

FIG. S11. **Self-diffusion coefficient in bulk water.** (a) Rigorous finite size scaling analysis of D_{S} vs. the inverse cubic box size L. (b) Extracted self-diffusion coefficient D_{S} at infinite system size as a function of the pressure P in the liquid phase. Simulations denote results from this work extracted in (a), experimental data are taken from Krynicki et al..[10]

To correct for the finite size of our cubic simulation box of length l, we follow the finite-size scaling approach by Yeh and Hummer to obtain the self-diffusion coefficient in an infinite nonperiodic system,[11]

$$D_{\mathrm{s}}^{(\mathrm{PBC})} = D_{\mathrm{s}}^{(\mathrm{bulk})} - \frac{k_{\mathrm{B}}T\xi}{\pi\eta_{\mathrm{b}}L}. \tag{S2}$$

Here, $D_{\mathrm{s}}^{(\mathrm{bulk})}$ is the self-diffusion coefficient in the non-periodic, infinite-size bulk liquid phase, whereas D_{PBC} is the corresponding value obtained in a finite, periodic simulation box. The thermal energy is $k_{\mathrm{B}}T$ and the shear viscosity is η_{b}.

Figure S11(a) shows the self-diffusion coefficient of bulk water determined from the mean square displacement for different densities in a constant volume and temperature (NVT) simulations, where the side length L is varied. The solid lines in Fig. S11(a) denote fits of the simulation data to Eq. (S2), revealing excellent agreement with the expected scaling L^{-1}. The corresponding extrapolated values $D_{\mathrm{s}}^{(\mathrm{bulk})}$ are shown in Fig. S11(b) as blue symbols and are practically independent of the pressure. During the fitting procedure, we fixed the value $\eta_{\mathrm{b}} = 0.695\,\mathrm{mPa\,s}$

independently of the density.[12] If we treat the η_b as free parameter during fitting, the resulting bulk viscosity independent of pressure within the fitting errors and independent of pressure in the considered range, $\eta_b^{(fit)} = 0.696 \pm 0.017\,\mathrm{mPa\,s}$, well in line with the literature,[12] and reflecting again the fact that water is incompressible in this pressure range. We also include in Fig. S11(b) the corresponding pressure-dependent water self-diffusion coefficient measure using the proton spin echo method.[10] Whereas the employed SPC/E water model over-estimates the water self-diffusion by about 30%, the fact that D_s is independent of pressure is well reflected within the experimental values.

[1] Colin Bousige, Camélia Matei Ghimbeu, Cathie Vix-Guterl, Andrew E. Pomerantz, Assiya Suleimenova, Gavin Vaughan, Gaston Garbarino, Mikhail Feygenson, Christoph Wildgruber, Franz-Josef Ulm, Roland J.-M. Pellenq, and Benoit Coasne. Realistic molecular model of kerogen's nanostructure. *Nature Materials*, 15(5):576–582, May 2016. ISSN 1476-4660. doi:10.1038/nmat4541.

[2] Anthony K. Rappe and William A. Goddard. Charge equilibration for molecular dynamics simulations. *J. Phys. Chem.*, 95(8):3358–3363, April 1991. ISSN 0022-3654. doi:10.1021/j100161a070.

[3] Adri C. T. van Duin, Siddharth Dasgupta, Francois Lorant, and William A. Goddard. ReaxFF: A Reactive Force Field for Hydrocarbons. *J. Phys. Chem. A*, 105(41):9396–9409, October 2001. ISSN 1089-5639. doi:10.1021/jp004368u.

[4] In-Chul Yeh and Max L. Berkowitz. Ewald summation for systems with slab geometry. *The Journal of Chemical Physics*, 111(7):3155–3162, August 1999. ISSN 0021-9606, 1089-7690. doi:10.1063/1.479595.

[5] Caroline Desgranges and Jerome Delhommelle. Benchmark Free Energies and Entropies for Saturated and Compressed Water. *J. Chem. Eng. Data*, 62(11):4032–4040, November 2017. ISSN 0021-9568. doi:10.1021/acs.jced.7b00753.

[6] W. Wagner and A. Pruß. The IAPWS Formulation 1995 for the Thermodynamic Properties of Ordinary Water Substance for General and Scientific Use. *Journal of Physical and Chemical Reference Data*, 31(2):387–535, June 2002. ISSN 0047-2689. doi:10.1063/1.1461829.

[7] Witold Brostow, Thomas Grindley, and M. Antonieta Macip. Volumetric properties of organic liquids as a function of temperature and pressure: Experimental data and prediction of compressibility. *Materials Chemistry and Physics*, 12(1): 37–97, January 1985. ISSN 0254-0584. doi:10.1016/0254-0584(85)90035-5.

[8] Jean-Paul Ryckaert, Giovanni Ciccotti, and Herman J. C Berendsen. Numerical integration of the cartesian equations of motion of a system with constraints: Molecular dynamics of n-alkanes. *Journal of Computational Physics*, 23(3):327–341, March 1977. ISSN 0021-9991. doi:10.1016/0021-9991(77)90098-5.

[9] Wataru Shinoda, Motoyuki Shiga, and Masuhiro Mikami. Rapid estimation of elastic constants by molecular dynamics simulation under constant stress. *Phys. Rev. B*, 69(13):134103, April 2004. doi:10.1103/PhysRevB.69.134103.

[10] Kazimierz Krynicki, Christopher D. Green, and David W. Sawyer. Pressure and temperature dependence of self-diffusion in water. *Faraday Discuss. Chem. Soc.*, 66(0):199–208, January 1978. ISSN 0301-7249. doi:10.1039/DC9786600199.

[11] In-Chul Yeh and Gerhard Hummer. System-Size Dependence of Diffusion Coefficients and Viscosities from Molecular Dynamics Simulations with Periodic Boundary Conditions. *J. Phys. Chem. B*, 108(40):15873–15879, October 2004. ISSN 1520-6106. doi:10.1021/jp0477147.

[12] Alexander Schlaich, Julian Kappler, and Roland R. Netz. Hydration Friction in Nanoconfinement: From Bulk via Interfacial to Dry Friction. *Nano Lett.*, 17(10):5969–5976, October 2017. ISSN 1530-6984. doi:10.1021/acs.nanolett.7b02000.

TOC Graphic

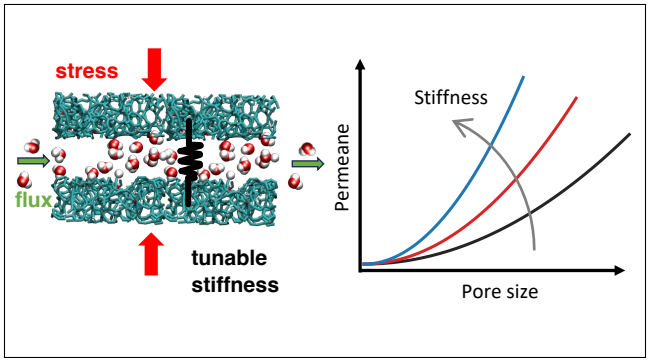
stress
flux
tunable
stiffness
Permeane
Stiffness
Pore size